Monthly Notices of the ROYAL ASTRONOMICAL SOCIETY

MNRAS **548,** 1–28 (2026) https://doi.org/10.1093/mnras/stag631
Advance Access publication 2026 April 02

The *Herschel*-SPIRE Dark Field III: probing the deepest *Herschel* field with SCUBA-2

Ayushi Parmar [1]★ David L. Clements [1] Chris Pearson [2,3,4] and Thomas W. O. Varnish [1,2,5]

[1]*Astrophysics Group, Department of Physics, Blackett Laboratory, Imperial College London, London SW7 2AZ, UK*
[2]*RAL Space, UKRI STFC Rutherford Appleton Laboratory, Chilton, Didcot, Oxfordshire OX11 0QX, UK*
[3]*Department of Physical Sciences, The Open University, Milton Keynes MK7 6AA, UK*
[4]*Oxford Astrophysics, Department of Physics, Denys Wilkinson Building, University of Oxford, Keble Road, Oxford OX1 3RH, UK*
[5]*Plasma Science and Fusion Center, Massachusetts Institute of Technology, Cambridge, MA 02139, USA*

Accepted 2026 March 24. Received 2026 March 10; in original form 2025 August 8

ABSTRACT

The *Herschel*-SPIRE Dark Field (SDF), originally observed for calibration of the SPIRE instrument, is the deepest far-infrared field to date (equivalent exposure time of $\sim 700\,\mathrm{h\,deg^{-1}}$) at wavelengths 250–500 μm, probing below the SPIRE confusion limit. We present SCUBA-2 850 μm observations covering the central Deep Region, detecting 36 sources with number counts consistent with previous surveys at this wavelength. Cross-identification with multiwavelength catalogues reveals 20 SPIRE-dropouts, whose stacked SPIRE fluxes suggest a photometric redshift of $z \sim 4$. Photo-z estimates from the MAGPHYS, BAGPIPES, and MMPZ tools are consistent within the uncertainties for 3 sources ($z \sim 1$–2), while 13 are inconsistent, and 20 lack sufficient data due to counterpart ambiguity or non-detections. We flag a total of 9 sources as potentially lensed and 15 as potential multiples. Spectral energy distribution fitting yields average properties for SPIRE-detected sources of $\log_{10}(L_{\rm FIR}/\mathrm{L}_\odot) = 13.6 \pm 0.1$, $\log_{10}(M_{\rm dust}/\mathrm{M}_\odot) = 8.1 \pm 0.1$, and $\mathrm{SFR_{obsc}} = 7000 \pm 1900\ \mathrm{M_\odot\,yr^{-1}}$. The stacked dropouts yield $\log_{10}(L_{\rm FIR}/\mathrm{L}_\odot) = 12.8^{+0.5}_{-0.7}[12.5^{+0.4}_{-0.6}]$, $\log_{10}(M_{\rm dust}/\mathrm{M}_\odot) = 6.52^{+0.33}_{-0.41}[6.71^{+0.19}_{-0.23}]$, and $\mathrm{SFR_{obsc}} = 700^{+1500}_{-560}[350^{+420}_{-250}]\ \mathrm{M_\odot\,yr^{-1}}$ at a derived $z = 6.7^{+2.4}_{-3.0}$ (at a fixed $z = 4.0^{+0.1}_{-0.6}$) contributing ~ 15 (~ 2) per cent of the cosmic star formation rate density (SFRD) at that epoch. We find an excess at $z \sim 1$ in the SFRD of SPIRE-detected sources, consistent with the sub-mJy bump in SPIRE number counts previously identified in this field, possibly tracing large-scale structure.

Key words: galaxies: evolution – galaxies: high-redshift – galaxies: photometry – cosmology: observations – submillimetre: galaxies.

1 INTRODUCTION

The cosmic infrared background contains the integrated history of obscured star formation (SF) and observations have shown that its total energy density is comparable to the Cosmic Optical Background (J. L. Puget et al. 1996; H. Dole et al. 2006; M. J. Devlin et al. 2009). The implications of this are significant; optical observations alone account for only about half of the total star formation rate (SFR) over the entire history of the Universe. With the arrival of large-scale submillimetre (submm) surveys, the discovery of a significant number of optically obscured galaxies [dusty star-forming galaxies (DSFGs)] challenged our understanding of galaxy formation and evolution (I. Smail, R. J. Ivison & A. W. Blain 1997; A. J. Barger et al. 1998; D. H. Hughes et al. 1998). This problem persists because current models and simulations are unable to reproduce the high-redshift ($z > 4$) population (C. D. Dowell et al. 2014; V. Asboth et al. 2016; R. Ivison et al. 2016), confirming that a notable component of the SFR density at high z is absent in ultraviolet-/optical-based studies. While several high-z DSFGs have been discovered (e.g. K. Coppin et al. 2006; E. Daddi et al. 2009; D. A. Riechers et al. 2010, 2013, 2021; P. L. Capak et al. 2011; F. Walter et al. 2012; C. D. Dowell et al. 2014; V. Asboth et al. 2016; Y. Fudamoto et al. 2017; J. Greenslade et al. 2019; J. Álvarez-Márquez et al. 2023), uncertainty still remains about their true contribution to the SFR density at $z > 3$ (V. Asboth et al. 2016). The fainter DSFG population, corresponding to intermediate or lower redshifts ($z < 2$), are key contributors to the dusty star-formation history at these lower redshifts but have proven difficult to study in large samples. The poor resolution of single-dish telescopes prevents the fainter population from being detected.

The most successful method to date for identifying high-z DSFGs has been the use of *Herschel*-SPIRE colours to identify sources that have spectral energy distributions (SEDs) that are still rising at 500 μm, ($S_{500} > S_{350} > S_{250}$), due to the large negative K-corrections at these wavelengths. These so-called 500 μm risers (C. D. Dowell et al. 2014) were inferred, and later confirmed to be, at high-z ($z > 4$), with the peak of their SEDs redshifted into submm wavelengths. Following this idea, a source with an

★ E-mail: a.parmar21@imperial.ac.uk

SED still rising at longer wavelengths of 850 μm could reside at an even higher redshift, defined as an 850 μm riser ($S_{850} > S_{500}$) (D. A. Riechers et al. 2017, 2021). However, the rarity of these 850 μm risers makes high-z DSFGs selection difficult.

Surveys of limited field size and depth have narrowed the search for candidate high-z sources to methods such as 500 μm riser selection, searching for lensed sources, or simply fortuitous discoveries. But with the arrival of larger area surveys at longer submm wavelengths (e.g. surveys such as the S2CLS; J. E. Geach et al. 2017 and S2-COSMOS; J. Simpson et al. 2019), new colour selection methods have opened up the search for even higher redshift DSFGs. Analysis of these source catalogues has revealed bright 850 μm sources that are undetected at both optical/NIR wavelengths and in any of the *Herschel*-SPIRE bands, suggestive of a high-z with a median redshift higher than the 500 μm riser population (e.g. J. Greenslade et al. 2019). An alternative explanation for a source to lack a SPIRE counterpart is that they represent a population of cooler sources that remain undiscovered at $z > 4$. Very few of these so-called 'SPIRE dropouts' have been studied in detail and the nature of this intriguing population remains uncertain. SPIRE-dropouts are suggested to account for ~ 20 per cent of all 850 μm sources (with signal-to-noise ratio, SNR > 5) in SCUBA-2 surveys (J. Greenslade et al. 2019). This implies that this high-z population is important for understanding the stellar mass build-up at earlier epochs, and confirming more high-z galaxies will allow us to determine to what extent this is the case.

The *Herschel* Space Observatory (G. L. Pilbratt et al. 2010) has completed a number of surveys using its onboard SPIRE instrument (M. J. Griffin et al. 2010), observing simultaneously at 250, 350, and 500 μm. At these wavelengths, however, SPIRE observations suffer from confusion due to the relatively low resolution and high number density of far-infrared (FIR) sources. Throughout its mission, *Herschel* regularly observed a dark patch of the sky for calibration purposes. Combining these observations together results in the *Herschel*-SPIRE Dark Field (SDF), the deepest FIR field available for the foreseeable future. C. Pearson et al. (2025) extracted SPIRE number counts for this field using two different source extraction techniques: SUSSEXtractor (R. S. Savage & S. Oliver 2007) and XID (P. Hurley et al. 2017). They found the SPIRE number counts to be in good agreement with the literature (e.g. S. J. Oliver et al. 2010, D. L. Clements et al. 2010, C. Pearson et al. 2017), with XID counts probing to fluxes a factor of 2 fainter than SUSSEXtractor. However, to probe even fainter fluxes ($\lesssim$ 1mJy), well below the confusion limit, statistical methods such as Probability of Deflection (P(D)) are required. T. Varnish et al. (2025) presented P(D) analysis of the SDF, which revealed a secondary peak in the SPIRE number counts at the faint-flux end. With current models unable to explain this secondary peak it became clear that further multiwavelength data, particularly sensitive submm observations, are required to probe both the resolved and unresolved DSFG population in this field.

In this paper, we present archival JCMT SCUBA-2 data at 850 and 450 μm, which overlap with the SDF, to study the submm regime and search for SPIRE counterparts. In Section 2, we describe the SCUBA-2 observations and data reduction process. In Section 3, we present our SCUBA-2 number counts, FIR/submm colour analysis, and compare photometric redshift estimates. We extract physical properties for our sample through FIR SED fitting and discuss the implications of our results in Section 4. We state our conclusions in Section 5.

2 OBSERVATIONS AND DATA REDUCTION

The SDF consists of overlapping wide and deep areas, located near the North Ecliptic Pole at RA $= 17^{\rm h}\ 40^{\rm m}\ 12^{\rm s}$, Dec. $= +69^{\circ}\ 00'\ 00''$ (C. Pearson et al. 2025). The entire SDF field spans a diameter of ~ 30 arcmin. It was observed regularly throughout the *Herschel* mission lifetime for calibration purposes, resulting in an extremely deep survey field. Within the SDF, a smaller 12 arcmin diameter region at the centre of the field is defined as the Deep Region where the P(D) analysis in T. Varnish et al. (2025) is performed. The Deep Region reaches an exposure time per square degree of at least 50 per cent deeper than the *Herschel* GOODS fields combined (I. Oteo et al. 2018). This makes the central region of SDF the deepest FIR field available for the foreseeable future.

In this paper, we work with two sets of archival SCUBA-2 observations:[1] Project ID M18AP049 (PI: J. Huang) and M20AP045 (PI: C. Cheng). Both data sets consist of 850 and 450 μm observations of the *Spitzer* IRAC Dark Field (J. Krick et al. 2009), which encompasses the entire Deep Region.

2.1 SCUBA-2 observations

We manually reduce the data following the procedure described in T. Cheng et al. (2019). This process is used for both 450 and 850 μm data, unless explicitly stated otherwise. Using the SCUBA-2 pipeline `SMURF` (E. L. Chapin et al. 2013), we use the `MAKEMAP` command on the individual scans from both observations for one wavelength. Within this command, the default `ITERATE` method is used to fit a number of models for noise and instrumental behaviour. The individual scans are then co-added using the `PICARD` recipe `MOSAIC_JCMT_IMAGES` to create a single map, as well as removing contaminant signals such as cosmic rays. In the next step, we crop the co-added maps using `CROP_SCUBA2_IMAGES` to a diameter of 16 arcmin. This removes the outer edge of each map where the noise dominates but still encompasses the entire Deep Region (central ~ 12 arcmin region).

Since we assume the SCUBA-2 sources to be unresolved point sources within the 850 μm beam [full width at half-maximum (FWHM) $= 14.6$ arcsec], we use the `PICARD` recipe `SCUBA2_MATCHED_FILTER` on the cropped maps in order to enhance the point sources. This recipe first smooths the input map and its generated point spread function (PSF) with a 30 arcsec FWHM Gaussian kernel and these smoothed maps are subtracted from the unsmoothed maps. These background-subtracted signal maps are then convolved with the PSF to produce the match-filtered signal maps. In parallel, the noise maps are also convolved with the PSF to produce the variance map. The match-filtered signal maps are in units of pW, and have to be calibrated using a flux correction factor (FCF) via `PICARD`'s `CALIBRATE_SCUBA2_DATA` recipe. We use the standard FCF value, as stated on the SCUBA-2/JCMT website,[2] of 537 ± 43 Jy beam^{-1} pW^{-1} for the 850 μm map and 491 ± 88 Jy beam^{-1} pW^{-1} for the 450 μm map. We note the 8 and 18 per cent FCF error of the 850 and 450 μm sources, respectively. Finally, we produce SNR maps from the calibrated maps using the `KAPPA` command, `MAKESNR`. Fig. 1 shows the fully reduced SCUBA-2

[1] https://www.cadc-ccda.hia-iha.nrc-cnrc.gc.ca/en/search/
[2] https://www.eaobservatory.org/jcmt/instrumentation/continuum/scuba-2/calibration/

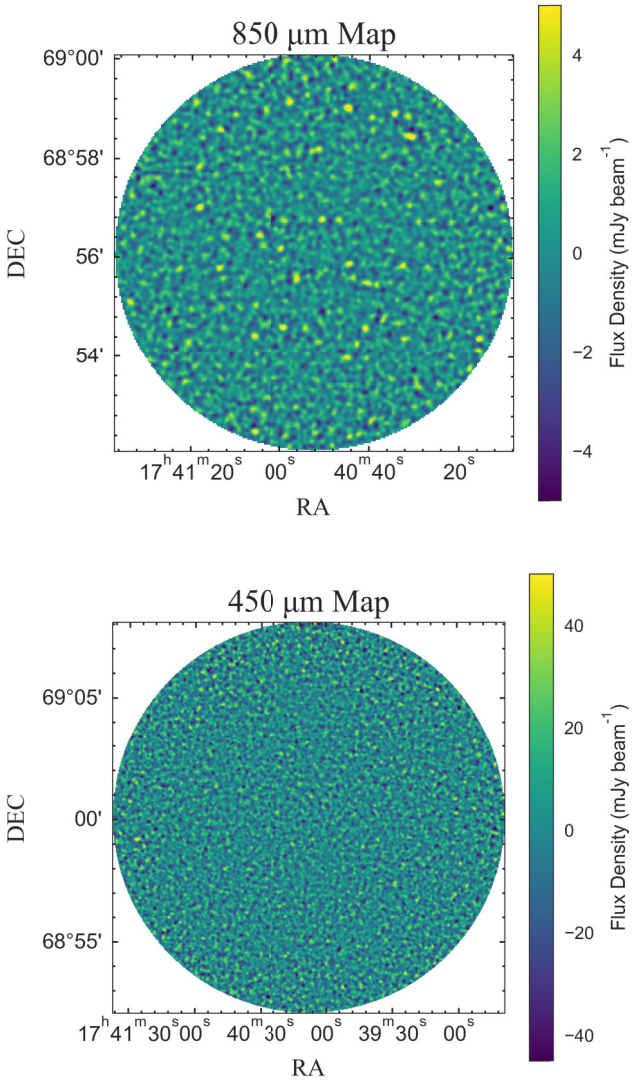

Figure 1. Fully reduced SCUBA-2 maps of the SDF at 850and 450 μm. Each map is 16 arcmin in diameter and encompasses the entirety of the Deep Region (central 12 arcmin diameter).

850 and 450 μm flux density maps. For the purpose of this paper, we focus on analysing only the 850 μm data.

2.2 Source extraction

To extract our 850 μm sources, we utilize the 850 μm SNR map and apply a simple peak-finding algorithm using the `find_peaks` function in the `astropyphotutils` package. With our input threshold SNR value of 4σ, local peaks are detected in the SNR map where a minimum separation of 4 pixels ($\approx$850 μm FWHM) is required between detected peaks. SCUBA-2 850 μm photometry has to be corrected for flux boosting, as investigated in J. E. Geach et al. (2017). They explore the effects of flux boosting in the SCUBA-2 Cosmology Legacy Survey (S2CLS) and find that the level of flux boosting is consistent across the whole survey area and can be well described by the following power law:

$$\frac{S_{\rm obs}}{S_{\rm true}} = 1 + 0.2\left(\frac{\rm SNR}{5}\right)^{-2.3}, \quad (1)$$

where SNR is the observed signal-to-noise ratio. To estimate the errors on our 850 μm flux density measurements, we use the 1σ measurement from the SNR map at the position of the peaks and add it in quadrature with the 850 μm FCF error stated earlier to get the total flux error. Once the total 850 μm flux error has been calculated for each source, we use equation (1) to deboost all our measured 850 μm fluxes and errors. To extract the 450 μm sources, we extract the 450 μm peak fluxes at the positions of the 850 μm detected peaks and use these sources as the initial 450 μm sample. Errors for the 450 μm fluxes are calculated similarly to the 850 μm flux errors. With this method, our initial sample consists of 36 detected 850 μm sources detected at $> 4\sigma$, each with a 450 μm flux constraint, however we note that there are no $> 3\sigma$ 450 μm counterparts.

2.2.1 *Reliability and completeness*

We study the reliability of our SCUBA-2 detected sources using two methods. First, we invert the flux density maps and use the same source detection method as earlier, which will find negative sources due to negative peaks. Assuming there are a similar number of spurious sources in the original map due to positive peaks, we calculate the ratio of the expected number of spurious sources to the number of detected positive sources to find the reliability. We find a reliability of 81.25 per cent at 4σ for 850 μm and 61 per cent at 3.5σ for 450 μm, corresponding to a flux limit of 3.3 and 12 mJy at 850 and 450 μm, respectively.

For our second method we create jackknife maps, where a random 50 per cent of the individual scans are inverted and co-added to the remaining individual scans; this produces maps that are effectively showing pure noise. Applying our source detection method to these maps, we find a reliability of 87.5 per cent at 4σ for 850 μm and a reliability of 78 per cent at 3.5σ for 450 μm.

To test how different SNR thresholds affect the reliability, we perform SNR cuts from 3–8σ and 2–8σ for 850 and 450 μm, respectively. Fig. 2 confirms that our initial 4σ detection threshold for 850 μm sources is suitable, and all sources with $> 5\sigma$ detections have 100 per cent reliability. We also find that there are no detected peaks above 4σ in the 450 μm map – hence the reliability is shown to fall to zero after this point (see Fig. 2) – and sources with detections between $3.5\sigma < \rm SNR < 4\sigma$ are the most reliable.

To evaluate the completeness of the sources, we insert a fixed number of fake sources ranging from 1 to 10 mJy into the 850 μm jackknife map and calculate the fraction that are recovered using the same source detection algorithm described above. We repeat this process 500 times for each flux bin. Following T. Cheng et al. (2019), the shape of our fake sources are circular 2D Gaussians, with a standard deviation equal to half of the SCUBA-2 FWHM at the wavelength being considered; FWHM at 850 μm is 14.6 arcsec. In Fig. 3 we show the estimated completeness of the 850 μm map as a function of the input flux density. The 850 μm map reaches a completeness of 50 per cent and 80 per cent at flux densities of $S_{850} \sim 4.32$ mJy and $S_{850} \sim 5.38$ mJy, respectively.

2.3 Ancillary data

Along with the SCUBA-2 observations, the SDF also overlaps with the IRAC Dark Field used for calibration purposes of the InfraRed Array Camera (IRAC; G. Fazio et al. 2004) on the *Spitzer Space Telescope* (M. W. Werner et al. 2004). This $\sim$ 20 arcmin diameter area provides four-band NIR (3.6, 4.5, 5.8, and 8 μm)

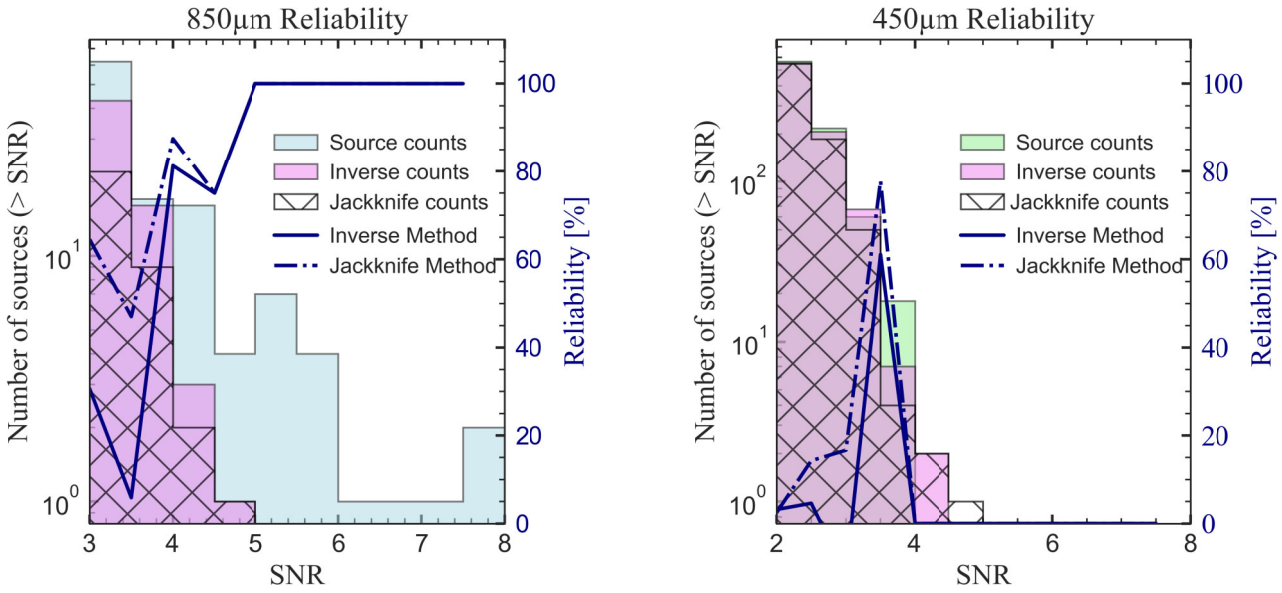

Figure 2. Reliability at 850 and 450 μm by comparing the number of sources in the science maps to the number of spurious detections above an increasing SNR threshold in the jackknife and inverted map. Results from both our methods are shown for comparison. 850 μm sources detected at 4σ and greater are the most reliable, with reliability rising to 100 per cent at 5σ. At 450 μm, the reliability of sources is highest at 3.5σ, after which the reliability falls to zero since no sources are detected at $> 4\sigma$.

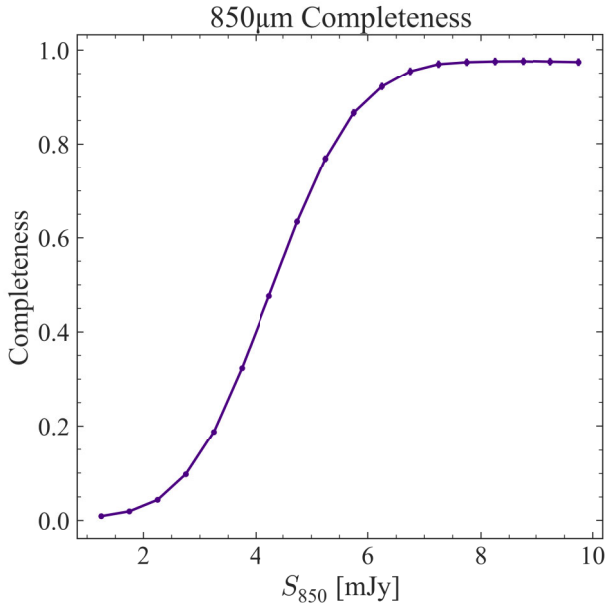

Figure 3. The 850 μm completeness for our Deep Region sample. Uncertainties are plotted but are very small. The 850 μm map reaches a completeness of 50 and 80 per cent at flux densities of $S_{850} \sim 4.32$ mJy and $S_{850} \sim 5.38$ mJy, respectively.

observations of the SDF. Optical to mid-IR observations of the concurrent IRAC Dark Field, detailed further in J. Krick et al. (2009), are also available; AKARI (11, 15, 18 μm; H. Murakami et al. 2007; T. Onaka et al. 2007), *Spitzer*-MIPS (24, 70 μm; G. Rieke et al. 2004), Palomar Hale LFC (u', g', r', z' ; R. Simcoe et al. 2000), and WIRC (*J, H, Ks*; J. C. Wilson et al. 2003), and *Hubble Space Telescope* (*HST*) ACS-WFC (*F*814*W*; H. C. Ford et al. 1998). A small rectangular region of the SDF has also been observed recently by *James Webb Space Telescope* (*JWST*) as part of the PEARLS programme (R. A. Windhorst et al. 2022), providing high-resolution NIR images at 1.5, 2.0, 3.56, and 4.44 μm. Cross-identification with this overlapping *JWST* data will be explored in future studies.

3 RESULTS

3.1 SCUBA-2 number counts

To investigate the source abundance in the Deep Region of the SDF, we calculate the integral and differential counts of the 850 μm detected sources. We sort the sources from brightest to faintest flux and count the cumulative number of sources at each 1 mJy step. To allow a comparison between the Deep Region and other literature data and models, we divide the number of sources by the area of our SCUBA-2 field (~ 0.06 deg^2) to obtain the number counts per square degree. Our results are stated in Table 1. Fig. 4 shows the cumulative integral counts and differential counts of the SPIRE Deep Region, compared with counts from previous works. Our 850 μm counts have been corrected for completeness, flux boosting, and reliability. We see that our Deep Region cumulative counts are largely consistent with the literature. In the faintest differential counts bin ($3 < S_\nu$[mJy] < 4, first boxed point in Fig. 4) the completeness falls to ~ 20 per cent (see Fig. 3), which is reflected by the downturn in the number counts at the faint end, making this faint flux bin unreliable. At fluxes $S_\nu > 4$ mJy, the completeness of the SDF sources is > 50 per cent and we see that the counts at the bright flux end (except at $S_\nu = 6.5$ mJy) agree within their uncertainties with the majority of the literature differential counts shown. We also see a dip in

Table 1. Corrected 850 μm number counts measured in the SPIRE Deep Region. Flux bins, ΔS are 1 mJy wide. The flux density, S, is the flux at the centre of each bin and $S' = S - 0.5\Delta S$. Uncertainties shown are Poissonian.

S [mJy]	$N(>S')$ [deg^{-2}]	dN/dS [deg^{-2} mJy^{-1}]
3.5	766.21 ± 117.0	182.63 ± 57.1
4.5	583.58 ± 102.1	202.75 ± 60.2
5.5	380.83 ± 82.5	190.93 ± 58.4
6.5	189.91 ± 58.2	21.68 ± 19.7
7.5	168.23 ± 54.8	95.52 ± 41.3
8.5	72.7 ± 36.03	72.21 ± 36.03

the counts at ~ 6.5 mJy (second boxed point in the plot) as only one source falls into that flux bin causing the differential counts to fall significantly below the literature counts at this flux. For the remaining (unboxed) points our differential counts are consistent (to 1σ) with the C.-C. Chen et al. (2013) and L.-Y. Hsu et al. (2016) models, and the K. Coppin et al. (2006) and C. M. Casey et al. (2013) results, all of which are also derived from SCUBA-2-selected 850 μm sources. Our counts and majority of the other literature counts lie modestly above those of J. E. Geach et al. (2017) in the intermediate flux bins. Given the consistent flux deboosting and completeness methodology between the works, the substantially smaller survey area of the SDF and the other literature works (on the order of arcmin^2) compared to the survey area of J. E. Geach et al. (2017) (~ 5 deg^2) is the most likely explanation for this discrepancy as field-to-field (cosmic) variance is expected to be much more significant for a smaller area.

3.2 SCUBA-2 – *Herschel* cross-identification

We explore whether our 850 μm sources have multiwavelength counterparts by cross-matching the detected sources with the XID catalogue generated by C. Pearson et al. (2025), which uses MIPS 24 μm positions as priors to extract SPIRE fluxes from the SPIRE maps. Before our search, we estimate SPIRE fluxes for each of our 850 μm sources by extracting the 250, 350, and 500 μm flux densities from the SPIRE maps at the position of the 850 μm source. The flux density errors are the 1σ confusion noise of the SPIRE instrument in each band (5.8, 6.3, 6.8 mJy at 250, 350, 500 μm). Then, we conduct a search for all possible matches between the 850 μm and C. Pearson et al. (2025) XID source positions, with a search diameter equal to the FWHM at 850 μm (14.6 arcsec). With this initial search, we find one or more XID sources located within the 850 μm beam centred on each source. To determine whether any of these XID sources are robust matches, we visually inspect the 850 μm map along with the SPIRE, 24 μm and IRAC 3.6 μm maps at the position of each 850 μm source and compare the XID position to the other wavelengths.We define two conditions that need to be satisfied for an XID source to be assigned as the 'correct' counterpart to an 850 μm source. The first condition requires the XID coordinates to coincide with the 250 μm SPIRE and 850 μm SCUBA-2 source on the map. To help make this determination, we also use the IRAC 3.6 μm map, which provides a higher resolution image of the XID source. The second condition requires our SPIRE flux estimates from the map to be comparable with the SPIRE XID fluxes. If both these conditions are met, we identify that XID source as the 24 μm counterpart to the 850 μm source. See the cut-outs of Sources 4, 14, and 29 in Fig. 5 for some examples of

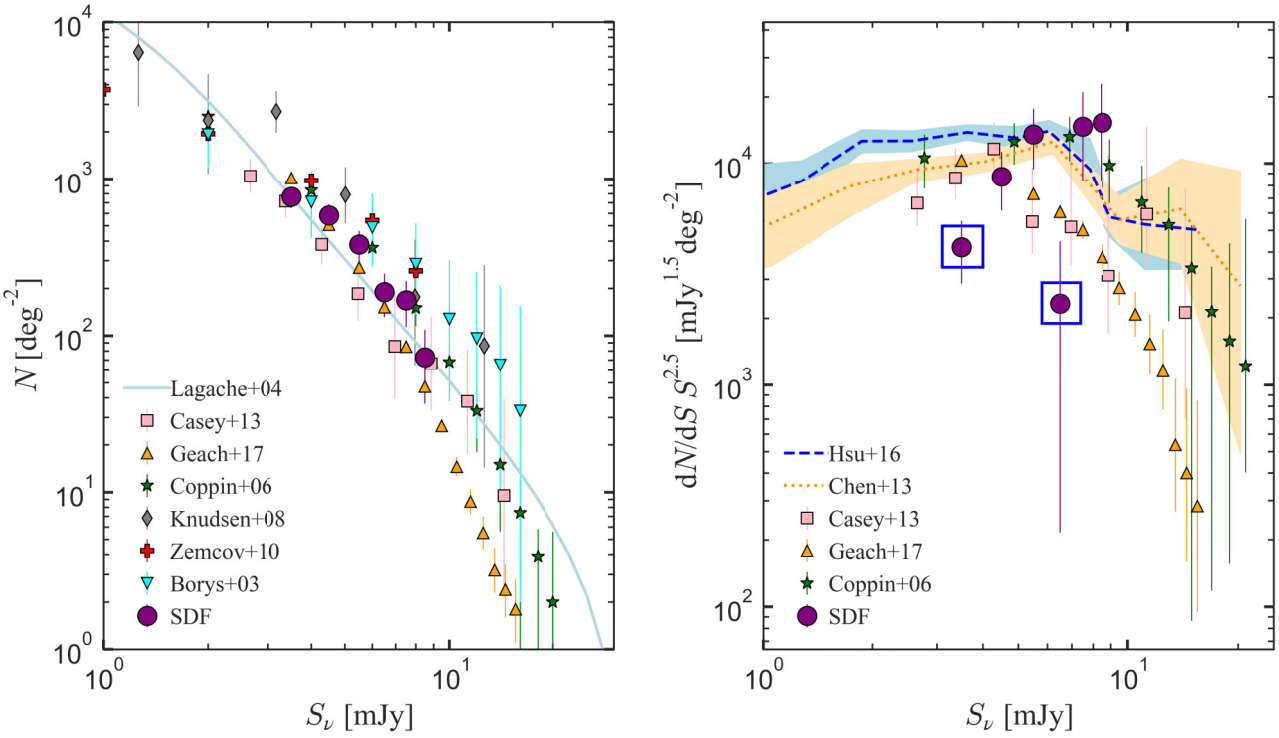

Figure 4. Number counts of the 850 μm detected sources. The left panel shows the cumulative number counts and the right panel shows the Euclidianized differential number counts. The 850 μm counts have been corrected for completeness, reliability, and flux-boosting. Both panels also show a selection of data (various coloured symbols) and two models (dashed and dotted lines) from the literature. The two boxed points in the right panel highlight specific bins in the differential counts that are discussed further in the text.

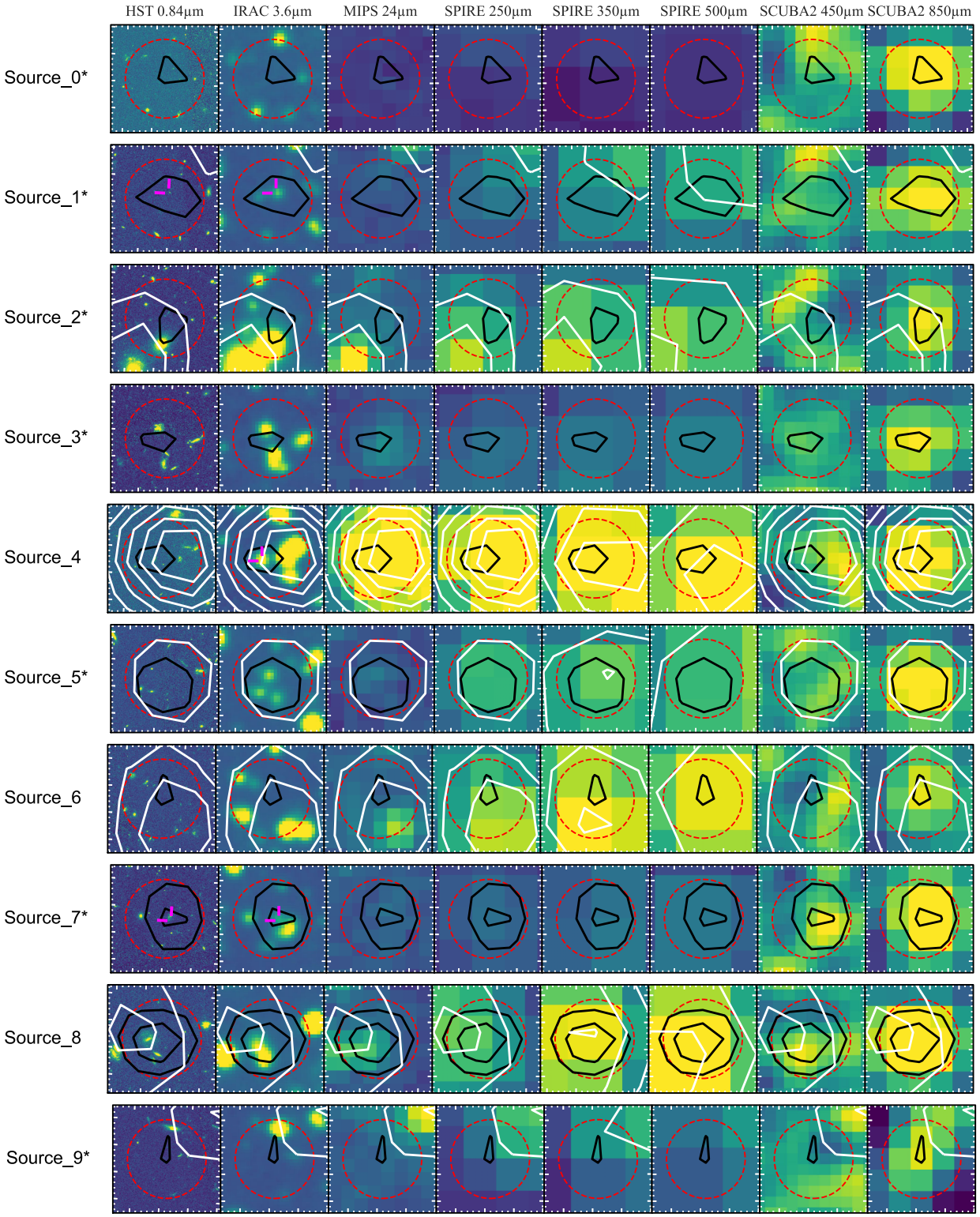

Figure 5. Multiwavelength 20 arcsec × 20 arcsec cut-outs of our 36 SCUBA-2 850 μm-detected sources. Images are shown from shortest to longest wavelength for the following bands; *HST* 0.84 μm, IRAC 3.6 μm, MIPS 24 μm, the three *Herschel*-SPIRE bands (250, 350, 500 μm) and the two SCUBA-2 bands (450, 850 μm). The dashed red circles signify the 850 μm FWHM (14.6 arcsec). The solid black contours signify the 850 μm 4–8σ contours in steps of 2σ. 1–5σ contours for each SPIRE band are shown on their respective images in solid white. The 250 μm contours are also overplotted on the *HST*, IRAC, MIPS, and SCUBA-2 images. In the cases where the white contours are not visible, the SPIRE source is $< 1\sigma$. Any *HST* and/or IRAC counterparts used in the photo-z analysis are marked with a pink crosshairs for the relevant sources. Sources marked with an asterisk next to their name are the sources we have categorized as SPIRE-dropouts. Note for Source_35, the position of the 850 μm source falls outside the dimensions of the *HST* image so the *HST* cut-out is left blank.

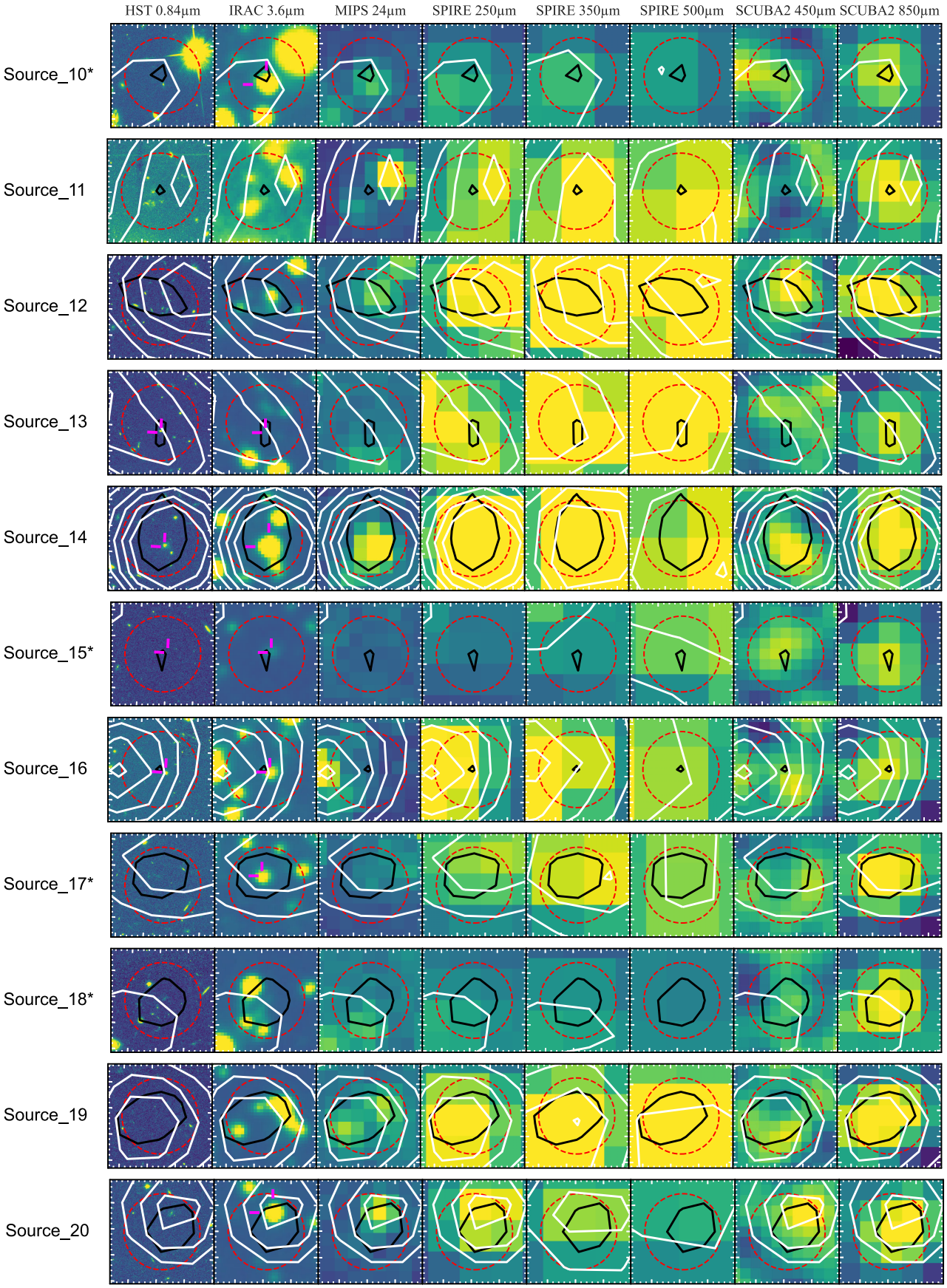

Figure 5. – *Continued*

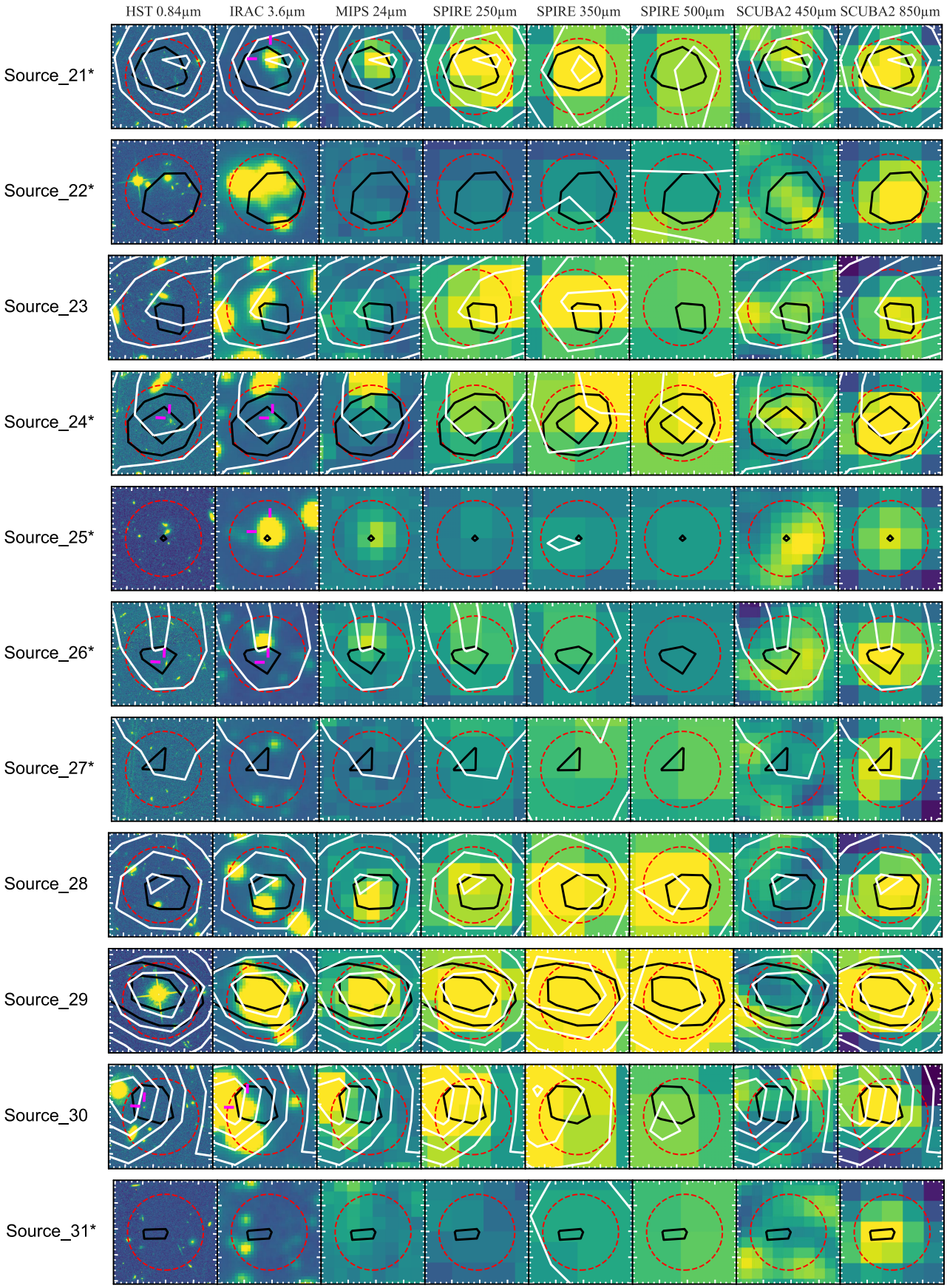

Figure 5. — *Continued*

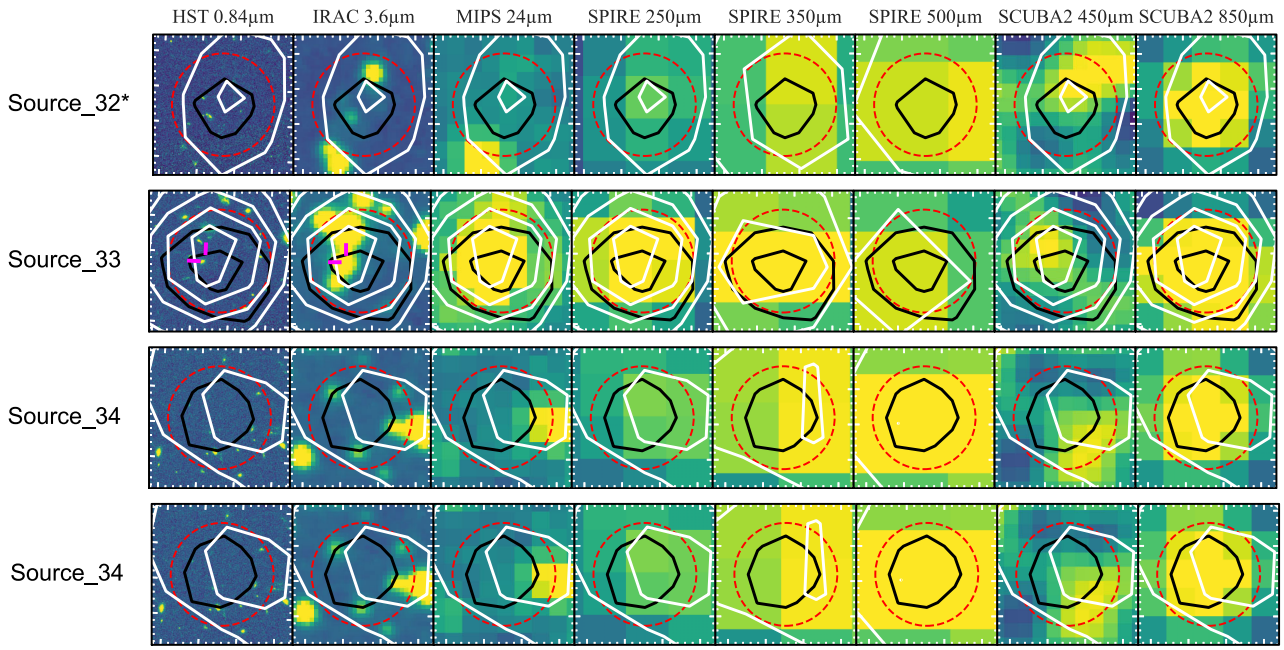

Figure 5. – *Continued*

good matches between the XID 24 μm and the 850 μm source. For any 850 μm sources where the first condition is not met, we assign these sources with our map-extracted SPIRE fluxes; these sources do not have an XID MIPS counterpart. See the cut-outs of Sources 19, 26, and 32 in Fig. 5 for some examples where the 24 μm source does not coincide with the 250 μm source.

As mentioned earlier, the J. Krick et al. (2009) catalogue provides optical–NIR coverage of the SDF as well as MIPS 24 μm data. MIPS sources that appear both in the J. Krick et al. (2009) catalogue and the C. Pearson et al. (2025) XID catalogue share the same ID. For sources for which we have identified a 24 μm XID counterpart, we extract the corresponding available optical–NIR photometry from the J. Krick et al. (2009) catalogue. In each case, we inspect the images to verify whether the NIR IRAC source from the catalogue corresponds to the 850 μm source position. For the sources where an XID MIPS counterpart was not identified in the previous steps, we cross-match the 850 μm source positions directly with the J. Krick et al. (2009) catalogue positions to identify any optical/NIR counterparts. Note that if an optical/NIR counterpart is identified, it does not correspond to a source in the XID catalogue and therefore these sources do not have an MIPS counterpart. In some cases there is a clear IRAC source that coincides directly with the 850 μm (and MIPS, if relevant) source. For example, see cut-outs of Sources 10, 20, 25 in Fig. 5. A few cases show multiple IRAC sources in and around the MIPS position making it difficult to identify a specific IRAC counterpart. For example, see cut-outs of Sources 14, 18, and 28. We discuss the sources with ambiguous IRAC counterparts in more detail in Section 3.4. Once we have extracted any available optical/NIR photometry, we discard any fluxes that are $< 5\sigma$ (i.e. any non-detections), to ensure the counterparts can be considered robust. These discarded optical/NIR fluxes, unless specified otherwise, are not included in the photo-z analysis in Section 3.4.

We next look for candidate SPIRE-dropouts in our sample by examining the 850 μm and SPIRE maps with their respective contours at the position of each 850 μm source. Those sources lacking a $> 3\sigma$ detection in SPIRE, we categorize as a SPIRE-dropout. For these dropouts, we update their SPIRE photometry to ensure they are assigned map-extracted SPIRE constraints; these are not flux measurements. These constraints can be treated as upper limits in subsequent analyses. We note that some of the sources we classify here as SPIRE-dropouts initially had assigned SPIRE fluxes from the XID catalogue as a result of the initial positional matching method described earlier. However, we find that for the SPIRE-dropouts with an identified XID counterpart, the XID SPIRE fluxes are comparable to the map-extracted SPIRE constraints and therefore remain undetected in SPIRE given the 3σ SPIRE confusion noise. There are some cases where the cut-outs show a $> 3\sigma$ SPIRE source within the 850 μm beam while the SPIRE map constraints suggest that the source is a SPIRE-dropout. The sources in question are Source 17, 20, 21, and 24, whose multiwavelength cut-outs are shown in Fig. 5, along with the cut-outs for the rest of our sample. This inconsistency in flux could be explained by the fact that the SPIRE constraints were extracted from the maps at the exact position of the SCUBA-2 source, which is not necessarily the brightest SPIRE pixel within the 850 μm beam. However, comparing the IRAC cut-outs to the rest of the wavelengths reveals more information about these sources. For Source_17 and Source_24 the IRAC bands show a source on the edge of the 850 μm contour, which seems to correspond to the position of the SPIRE detection (and also to a $> 1\sigma$ 450 μm source for Source_17) but does not correspond to the position of the 850 μm source. For Source_21, there are three potential IRAC counterparts (one bright and two faint) to the SPIRE source so we cannot say for certain which is the correct match and whether or not it corresponds to the 850 μm source. Closer inspection of Source_20 shows only one IRAC source within the 850 μm beam, which corresponds to the position of the MIPS, SPIRE, 450 μm, and 850 μm source. Based on these inspections, we decide to categorize Source_17, 21, and 24 as

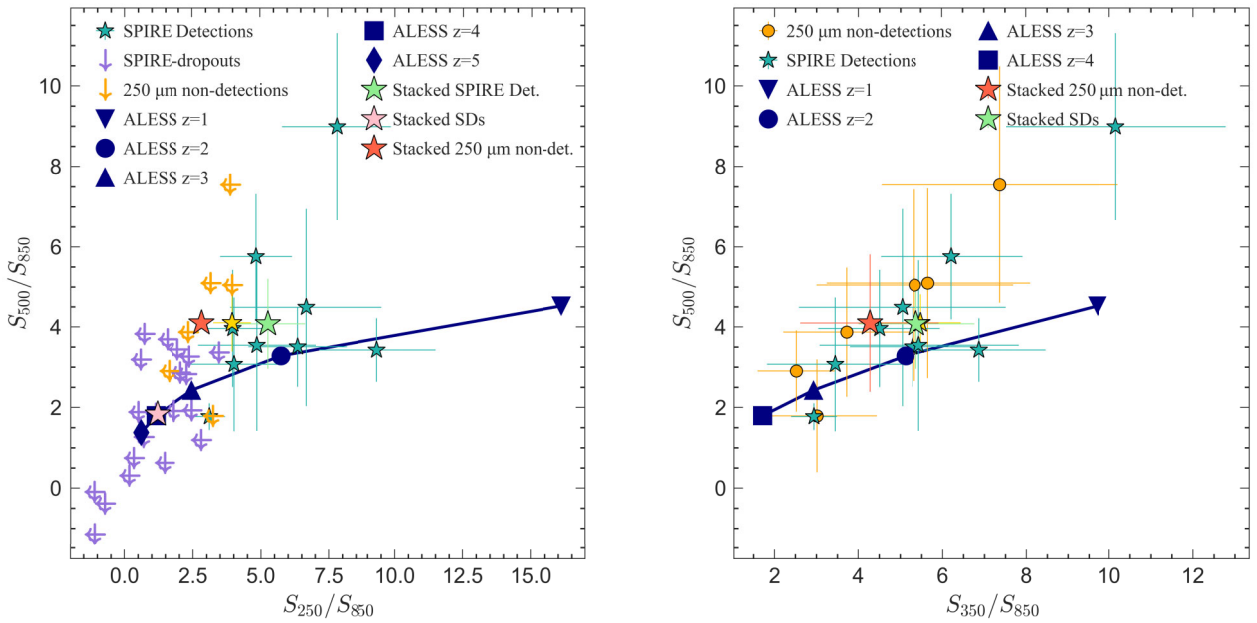

Figure 6. **Left:** S_{250}/S_{850} versus S_{500}/S_{850} colours of our SCUBA-2 sample with sources split into three different categories. The SPIRE-dropouts (i.e. lacking a SPIRE detection in any SPIRE band) are plotted as purple arrows, emphasizing that they are limits. The ratios for the SPIRE-dropouts are calculated using the flux constraints extracted from the SPIRE maps at the position of the SCUBA-2 source, hence we get some negative fluxes. The SPIRE-detected sources make up the remaing two categories; sources detected at 250 μm SPIRE are plotted as teal stars, while those sources that are non-detections at 250 μm but *are detected* at 350/500 μm are plotted as orange arrows. The colour-track of the average ALESS SED is overlaid for different redshifts. The SPIRE-dropouts tend to lie towards the bottom left corner of the plot, corresponding to higher redshifts. The average colour ratios of each group are also plotted. **Right:** We take the six orange sources in the left diagram and plot their S_{350}/S_{850} versus S_{500}/S_{850} colours, shown here as orange circles. These sources have non-detections at 250 μm but are detected at 350/500 μm. The ALESS SED colour-track is overlaid here as well. We also plot the S_{350}/S_{850} versus S_{500}/S_{850} colours of the sources that are detected in all SPIRE bands, shown in the teal stars. The average colour ratios of each group are also plotted, labelled as 'Stacked'. The yellow star in both panels corresponds to the SPIRE-detected Source_29, which we associate with a stellar object.

SPIRE-dropouts and we keep Source_20 categorized as a SPIRE-detected source.

After our categorization, we find a total of 20 SPIRE-dropouts in our SCUBA-2 sample – some of which have an identified optical/NIR counterpart – meaning > 50 per cent of our sample are SPIRE-dropouts. All SPIRE-dropout sources mentioned from here onwards will be marked with an asterisk (∗) next to their name. These SPIRE-dropouts are candidate high-z galaxies that are suggested to account for ∼ 20 per cent of all 850 μm sources (with SNR > 5) in SCUBA-2 surveys (J. Greenslade et al. 2019). The implication is that this high-z population is important for understanding the stellar mass build-up at earlier epochs. An alternative explanation for a source to lack a SPIRE counterpart is that it is instead a low-z non-thermal source. However, we can discount this possibility given that all of our SPIRE-dropout candidates lack a > 3σ radio counterpart in the 144 MHz LOFAR data available for this field (obtained through private communication; depth of ∼ 100 μJy), confirming they cannot be low-z non-thermal sources and reinforcing the idea that they are good high-z candidates. The remaining 16 sources include those with an XID and/or optical/NIR counterpart, and those without an identified counterpart. The multiwavelength cut-outs for each source are shown in Fig. 5.

In our 850 μm sample, we associate one source with a stellar object. The cut-outs of Source_29 show a bright source visible at all wavelengths (except 450 μm), but it becomes more obvious from the diffraction spikes seen in the *HST* cut-out that the object is stellar. We confirm the stellar classification of this source through a *Gaia* archive search.[3] From the *Gaia* archive, we also obtain a range of properties including effective temperature (∼ 4440 K), distance (∼ 1 kpc), parallax, and proper motion. This star poses an interesting question; is the star simply a very close chance alignment with the FIR source or could the star be associated with the FIR emission. We discuss this source further in Section 3.5.

3.3 Colour–colour diagrams

We use the SPIRE and SCUBA-2 fluxes of our sources to examine the FIR/submm colours of our sample. This method is often used as a rough redshift indicator for FIR/submm sources (e.g. D. Clements et al. 2014; C. D. Dowell et al. 2014; R. Ivison et al. 2016; J. Greenslade et al. 2018). Generally, a source with a rising SED in the FIR/submm regime will tend to lie at higher redshifts (C. M. Casey, D. Narayanan & A. Cooray 2014).

In the left panel of Fig. 6, we plot S_{250}/S_{850} versus S_{500}/S_{850} for our whole sample. In this panel, we split our sample into three different categories. The SPIRE-dropouts (i.e. lacking a SPIRE detection in any SPIRE band) are plotted as purple arrows, emphasizing that they are limits. As mentioned in Section 3.2, the SPIRE 'fluxes' of our SPIRE-dropouts are actually flux constraints that are extracted by reading off the flux from the SPIRE maps

[3] https://gea.esac.esa.int/archive/

at the position of the SCUBA-2 source. Since they are SPIRE-dropouts, some of the sources have unphysical negative fluxes. The SPIRE-detected sources make up the remaing two categories: sources detected at 250 μm (as well as 350/500 μm) are plotted as teal stars, while those sources that are non-detections at 250 μm but *are detected* at 350/500 μm are plotted as orange arrows since their S_{250}/S_{850} versus S_{500}/S_{850} colours will be inaccurate due to their non-detection at 250 μm. We also overlay the colour-track of the ALESS average SED (E. Cunha et al. 2015) at various redshifts for reference, originating from ALMA follow-up observations (J. Hodge et al. 2013; A. Karim et al. 2013) of the LABOCA ECDFS Submillimeter Survey (LESS; A. Weiß et al. 2009; J. L. Wardlow et al. 2011; R. C. Hickox et al. 2012). In this plot, the SPIRE-dropout candidates largely lie towards the higher redshift end (bottom left corner), with a handful of dropouts in the $z > 5$ region, confirming their initial high-z categorization. The sources with SPIRE detections largely lie at $z \lesssim 3$. The orange sources plotted in the right panel in Fig. 6 correspond to the same orange sources plotted in the left panel. Since these sources lack a 250 μm detection, we analyse their S_{350}/S_{850} versus S_{500}/S_{850} colours to get a better indication of their redshift. An ALESS average SED colour-track is also overlaid. Comparing the orange points in the left and right panels, we see that the S_{350}/S_{850} versus S_{500}/S_{850} colours have an overall lower redshift estimate than the S_{250}/S_{850} versus S_{500}/S_{850} colours. We also plot S_{350}/S_{850} versus S_{500}/S_{850} for the SPIRE-detected sources, also shown here as teal stars. These also largely lie at $z \lesssim 3$, in agreement with their S_{250}/S_{850} versus S_{500}/S_{850} colours.

Using the colour ratios of individual sources, we calculate the average colours of each category, shown by the 'Stacked' points in Fig. 6. Studying the SPIRE-dropouts, we find that the upper limit of the average S_{250}/S_{850} versus S_{500}/S_{850} ratio favours redder colours. For the same ratio, the SCUBA-2 sources with SPIRE detections favour bluer colours, highlighting the clear difference between the higher and lower z nature of SPIRE-dropouts and SPIRE-detections, respectively. In-between these two categories we find the average S_{250}/S_{850} versus S_{500}/S_{850} ratio for 250 μm non-detections, albeit located closer to the bluer end of the colour-colour diagram; a trend that is also seen in the S_{350}/S_{850} versus S_{500}/S_{850} plot.

3.4 Photometric redshifts

We find no spectroscopic redshifts for any sources in our SDF sample so we use the range of available multiwavelength data to estimate photometric redshifts for our SCUBA-2 sources. We first use the MAGPHYS + PHOTO-Z (Multi-wavelength Analysis of Galaxy Physical Properties + Photometric redshift; A. Battisti et al. 2019) tool to estimate a photometric redshift for all sources that have an identified optical/NIR counterpart. For these MAGPHYS runs we use the full optical/NIR–submm photometry. Our results our stated in Table 4 under MAGPHYS ($z_{\rm all}$). This value reflects the median of the best-fitting model's probability density function (PDF), with uncertainties reflecting the 16–84$^{\rm th}$ percentile; we use this MAGPHYS redshift in the following comparison. The bracketed MAGPHYS value reflects the redshift of the best-fitting MAGPHYS model. Our second tool is the latest version of the code BAGPIPES (Bayesian Analysis of Galaxies for Physical Inference and Parameter EStimation; A. Carnall et al. 2018), with our input parameters for the code listed in Table 2, and the redshift fixed to the MAGPHYS estimate. We perform two sets of BAGPIPES runs for sources with an identified shorter wavelength counterpart. The first run uses only the optical–NIR photometry of the identified counterpart (BAGPIPES $z_{\rm opt/NIR}$ in Table 4), while the second run uses the full optical/NIR–submm photometry (BAGPIPES $z_{\rm all}$ in Table 4). For both BAGPIPES runs we state the median value and error, reflecting the 16–84th percentiles of the BAGPIPES posterior.

Table 2. List of input parameters for our BAGPIPES runs.

BAGPIPES			
Global	Delayed SFH	Dust	Nebular
$0 < z < 10$	$0.1 < \tau$ [Gyr] < 10	D. Calzetti et al. (2000)	$-4 < \log_{10}(U) < -2$
	$0.01 < \alpha < 1000$	$0 < A_v < 8$	
	$0.01 < \beta < 1000$		
	$0 < Z_\odot < 2.5$		

We had previously discarded any optical/NIR photometry that were non-detections (i.e. $< 5\sigma$); however, there are certain sources where the non-detections are included in the photo-z estimations and this is explicitly stated for each relevant case. Since MAGPHYS does take upper limits into account, we set the flux of these non-detections to zero and set the uncertainty as the 3σ upper limit. BAGPIPES does not take upper limits into account so for the non-detections we simply input the flux constraint and corresponding error. See Appendix A for the final catalogue of fluxes used to calculate the photo-z estimates. Although we do not show the cut-outs of all the optical/NIR bands in the final catalogue, photometry from all detected bands are included in the photo-z estimation.

Finally, we use MMPZ (The millimeter photometric redshift tool; C. M. Casey 2020) to constrain the photometric redshifts of all our sources using only their FIR/submm fluxes. We note that since the SPIRE flux-constraints are used for the MMPZ redshift estimates of the SPIRE-dropout sources (marked with an asterisk in Table 4), these estimates are shown as lower limits. The rest of the MMPZ results reflect the mode of the $P(z)$ distribution and the upper/lower bound of the 68 per cent minimum credible interval. In Fig. 7 we show the best-fitting SED from MAGPHYS and the two BAGPIPES runs, stating the best-fitting redshift for each source. Corresponding PDFs from MAGPHYS, BAGPIPES and MMPZ are also shown. We verified that all redshift probability distributions were normalized such that $\int P(z)dz = 1$; when necessary, distributions were renormalized before further analysis.

To compare the photometric redshift estimates of the sources with an identified counterpart, we consider a source as having a 'Consistent photo-z' if all four of its redshift estimates are consistent within the respective uncertainties. If all four redshift estimates are not consistent within the uncertainties, we group them under 'Inconsistent photo-z'. Note that for the SPIRE-dropouts, we compare the MMPZ lower limit to the remaining three redshifts. A caveat to our chosen criteria is that if a source is grouped as consistent, it means that the optical and FIR regimes agree therefore the optical source is suggestive of being the correct counterpart to the FIR source and so there is no strong evidence of it being a lens. However, this does not mean that the estimated redshift is robust and reliable. Rather, our aim is to identify sources that are definitely inconsistent and therefore are likely to be lenses. For the remaining sources that do not have an optical/NIR counterpart or if the ability to make a cross-ID is hindered by source-blending or multiple candidate IDs, we classify under 'Insufficient Data'. Fig. 5 shows the multiwavelength

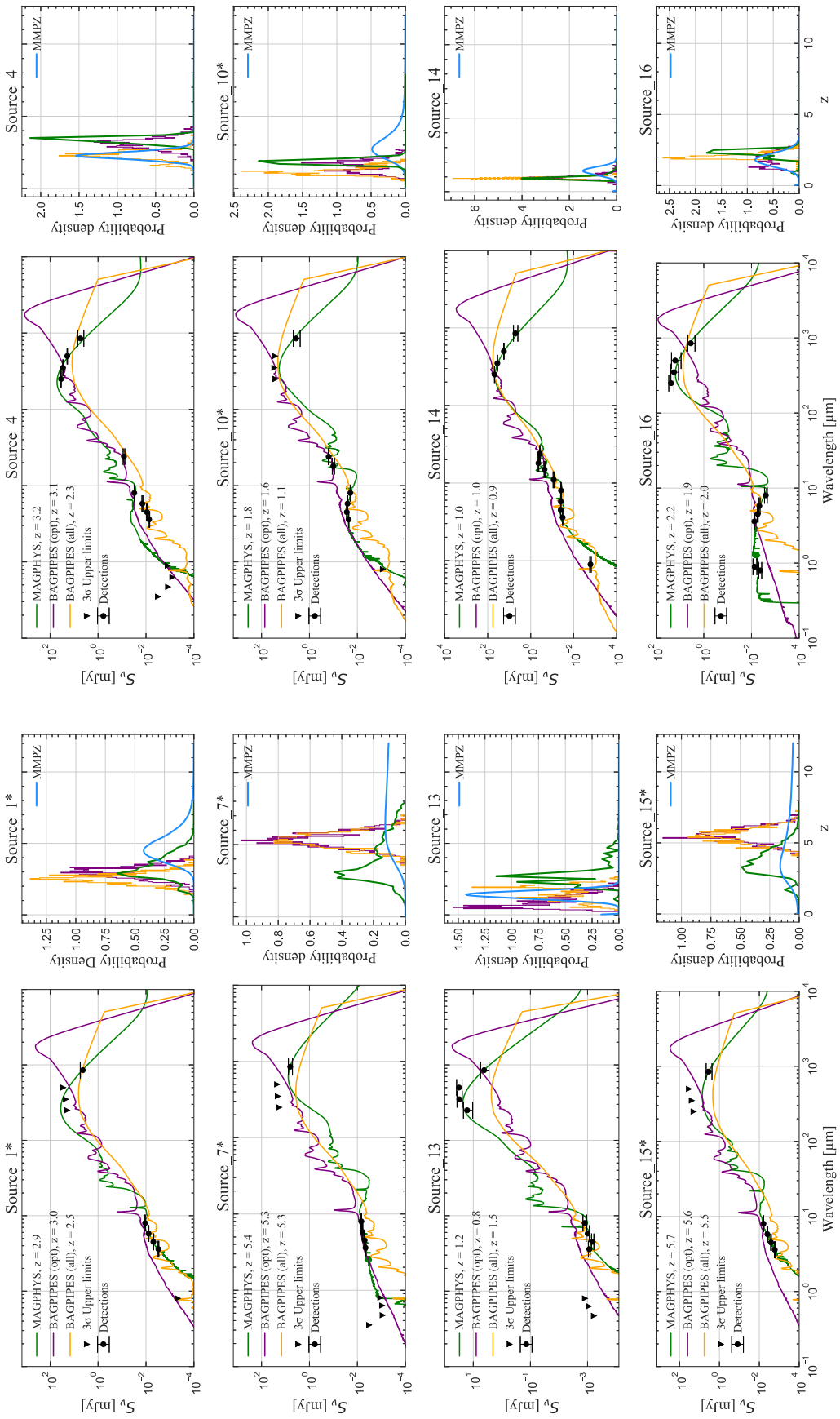

Figure 7. For the 16 sources in Table 4 that make up the consistent and inconsistent groups, we show here the best-fitting MAGPHYS SED using optical-submm photometry (green), the best-fitting BAGPIPES SED using optical–NIR photometry [BAGPIPES (opt) in purple], and the best-fitting BAGPIPES SED using optical–submm photometry [BAGPIPES (all) in orange]. Also stated is the best-fitting redshift for each fit. Detections and 3σ upper limits are overplotted in black. Each SED plot has a corresponding redshift PDF. The legend for MAGPHYS and BAGPIPES in the SED plots also apply to the probability density plots. Additionally shown is the MMPZ PDF in blue. Sources whose names are marked with an asterisk (∗) are SPIRE-dropouts.

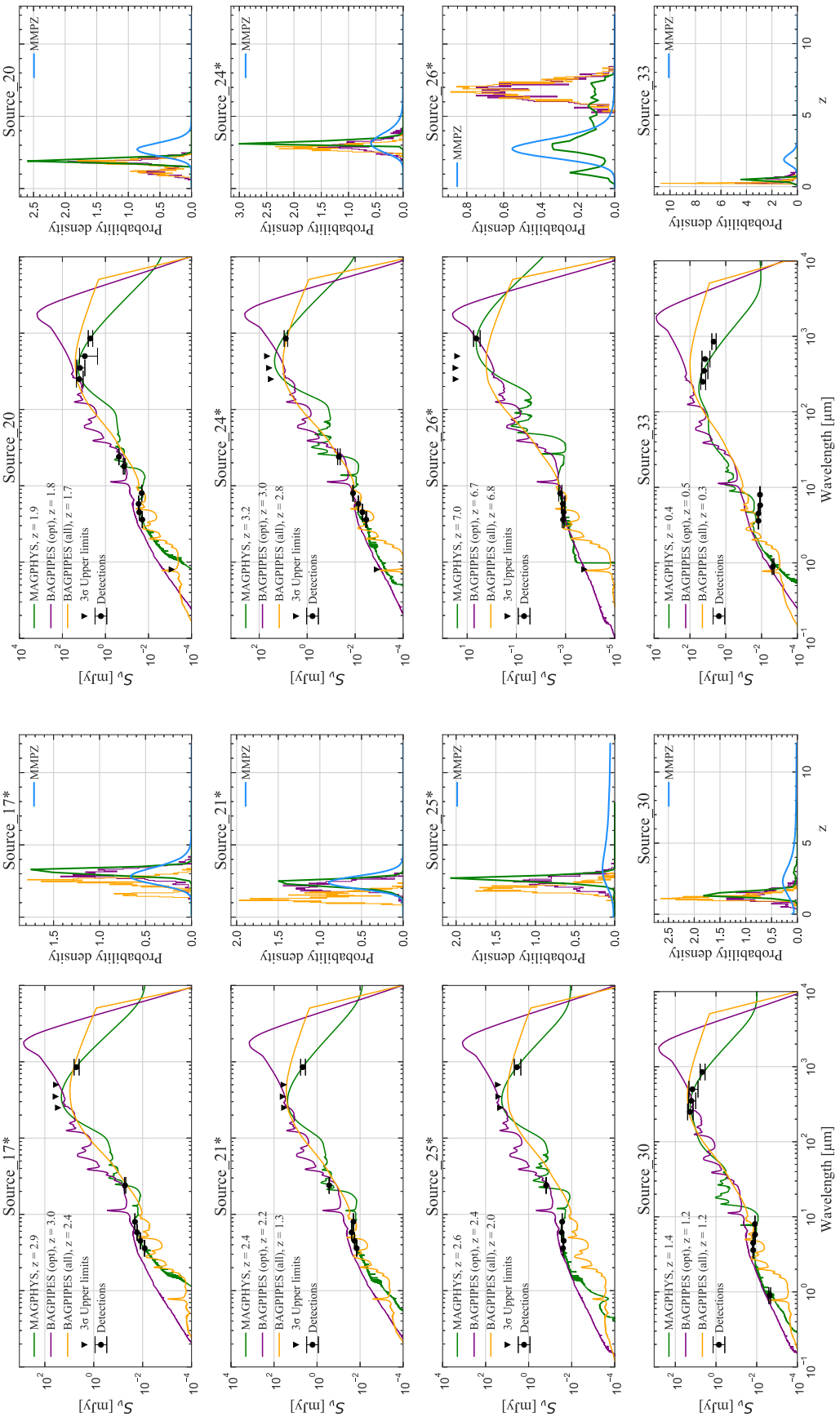

Figure 7. — *Continued*

cut-outs that we use to obtain our cross-IDs. Below, we discuss the photo-z results from our various methods for each source. For the relevant sources with an identified shorter wavelength counterpart, the *HST* and/or IRAC counterpart used in the photo-z calculation is marked with a pink crosshairs in the Fig. 5 cut-outs. Source names that are marked with an asterisk are our candidate SPIRE-dropouts. Our photo-z results are tabulated in Table 4. best-fitting SEDs and redshift PDFs for each source are shown in Fig. 7.

3.4.1 Consistent photo-z:

Source_14: A bright SPIRE-detected source with a clear counterpart in MIPS. The MIPS source could be a blend of three IRAC sources, all of which are clearly distinct in *HST*. Positionally, the MIPS source coincides with the central IRAC source and the MAGPHYS photo-z estimate for this cross-ID is $z = 0.9^{+0.1}_{-0.1}$. Both BAGPIPES runs, $z_{\rm opt/NIR} = 1.0^{+0.2}_{-0.1}$ and $z_{\rm all} = 0.9^{+0.1}_{-0.1}$, and the MMPZ run, $z = 1.4^{+0.2}_{-0.4}$, all agree with MAGPHYS. To investigate the possible multiplicity of this source, we estimate the optical/NIR BAGPIPES photo-z of the surrounding two IRAC sources. The upper and lower IRAC sources have BAGPIPES estimates of $z = 1.4^{+1.9}_{-0.7}$ and $1.3^{+2.2}_{-0.6}$, which is consistent within uncertainties with the photo-z estimates of Source_14 stated in Table 4, suggesting that the IRAC sources may be physically associated. We cannot be certain that the surrounding IRAC sources do not contribute to the FIR flux of the 850 μm source as well and so we classify this source as a potential multiple. Spectroscopic observations will be needed to confirm this.

Source_16: This source has a visible IRAC and *HST* counterpart located 1.4 arcsec away from the 850 μm position, but no MIPS counterpart. MAGPHYS estimates a photo-z of $z = 2.2^{+0.2}_{-0.2}$. Both BAGPIPES runs, $z_{\rm opt/NIR} = 1.9^{+0.5}_{-0.6}$ and $z_{\rm all} = 2.0^{+0.2}_{-0.1}$, are in agreement with MAGPHYS, as is the MMPZ estimate of $z = 1.8^{+0.4}_{-0.5}$. Although these photo-z estimates are deemed consistent, the offset between the optical/NIR source and the 850 μm source position could suggest lensing. However, higher resolution submm/mm data are required to confirm this. We classify this source as potentially lensed.

Source_30: An *HST* source is visible within the 850 μm contour, which also has an IRAC counterpart in the catalogue. With this counterpart, MAGPHYS estimates $z = 1.4^{+0.3}_{-0.2}$. BAGPIPES estimates $z_{\rm opt/NIR} = 1.2^{+0.4}_{-0.3}$ and $z_{\rm all} = 1.2^{+0.2}_{-0.2}$, while MMPZ estimates $z = 2.3^{+1.8}_{-1.5}$. All estimates are consistent with each other within the uncertainties. We note that the *HST* source used here is 3.8 arcsec away from the 850 μm position, so lensing could be a possibility; however, higher resolution data are needed to confirm this. We classify this source as likely lensed.

3.4.2 Inconsistent photo-z:

Source_1∗: A SPIRE-dropout with two potential IRAC counterparts, each with its own optical counterpart. The position of the brighter, central IRAC source is consistent with the 850 μm source position. For this counterpart, we include the *HST* constraint ($< 5\sigma$) in our fits since we clearly see the *HST* source in the cut-outs. MAGPHYS estimates $z = 3.2^{+1.0}_{-0.6}$. With BAGPIPES we get $z_{\rm opt/NIR} = 3.0^{+0.4}_{-0.4}$ and $z_{\rm all} = 2.5^{+0.4}_{-0.4}$. These estimates are not consistent with the MMPZ lower limit of $z > 4.5$. The second, fainter IRAC source is 2.5 arcsec from the 850 μm position and has a BAGPIPES photo-z estimate of $z = 4.8^{+1.7}_{-2.0}$, which is consistent with the estimate of the bright IRAC source and the MMPZ limit. Hence, there is a possibility that the two IRAC sources are physically associated, but we require higher resolution long wavelength data to confirm this. We classify this source as a potential multiple.

Source_4: A bright SPIRE-detected source with a clear counterpart in MIPS and IRAC. The *HST* catalogue counterpart to the IRAC source is $< 5\sigma$ and since there are two *HST* sources visible within the 850 μm contour in the cut-outs, we exclude the *HST* flux from our estimates. The estimate from MAGPHYS is $z = 3.4^{+0.1}_{-0.2}$, and from BAGPIPES we get $z_{\rm opt/NIR} = 3.1^{+0.3}_{-0.4}$ and $z_{\rm all} = 2.3^{+0.3}_{-0.4}$. MMPZ estimates $z = 2.3^{+0.2}_{-0.3}$. Within the uncertainties, these estimates are not all consistent with each other. We note that the SPIRE contours are offset from the 850 μm contours, and the cut-outs suggest that this SPIRE source corresponds to a different NIR source located to the right of the 850 μm counterpart. For this second IRAC source, BAGPIPES estimates a photo-z of $z = 2.7^{+0.9}_{-0.9}$, suggesting that the two IRAC sources could be physically associated and that it is likely they both contribute to the SPIRE/850 μm flux. Without higher resolution data, we cannot say for certain. This source is classified as a potential multiple.

Source_7∗: A SPIRE-dropout with an IRAC and *HST* counterpart but no MIPS counterpart. We include the $< 5\sigma$ optical fluxes since we can clearly see the optical source in the *HST* cut-out. We get a MAGPHYS estimate of $z = 3.6^{+2.0}_{-0.9}$. Although this agrees with the BAGPIPES estimates, $z_{\rm opt/NIR} = 5.3^{+0.5}_{-0.5}$ and $z_{\rm all} = 5.3^{+0.5}_{-0.5}$, all these estimates are inconsistent with the MMPZ lower limit of $z > 6.5$.

Source_10∗: A SPIRE-dropout that appears to have MIPS, IRAC, and *HST* counterparts. With MAGPHYS we estimate $z = 1.8^{+0.2}_{-0.1}$, and with BAGPIPES we estimate $z_{\rm opt/NIR} = 1.6^{+0.4}_{-0.5}$ and $z_{\rm all} = 1.1^{+0.3}_{-0.2}$. These estimates are all inconsistent with the MMPZ lower limit of $z > 2.7$. There is a 1.7 arcsec offset between the optical source position and the 850 μm source position, suggestive of lensing. With no other clear evidence of lensing in the cut-outs, higher resolution data are needed to determine the true nature of this source. We classify this source as potentially lensed.

Source_13: A bright SPIRE-detected source with no counterpart in MIPS but has a faint IRAC and a clear *HST* counterpart. The optical fluxes are $< 5\sigma$ but we include them – except the u-band flux, which is $\sim 0.1\sigma$ – in our MAGPHYS runs since the IRAC source is a robust detection and we see the *HST* source clearly in the cut-outs. MAGPHYS estimates a photometric redshift of $z = 2.7^{+0.7}_{-0.5}$. Holding this as a fixed redshift for the two BAGPIPES runs, we find that only the latter of the following estimates, $z_{\rm opt/NIR} = 0.8^{+0.5}_{-0.3}$ and $z_{\rm all} = 1.5^{+0.6}_{-0.5}$, are consistent with MAGPHYS within the uncertainties. The MMPZ estimate of $z = 2.3^{+1.8}_{-1.5}$ is consistent with the other methods but since the four estimates are not all consistent within the uncertainties, we group this source as inconsistent.

Source_15∗: A SPIRE-dropout with a faint counterpart visible in the IRAC and *HST* bands. MAGPHYS estimates a photo-z of $z = 3.6^{+1.0}_{-0.8}$. This is inconsistent with the following two BAGPIPES estimates of $z_{\rm opt/NIR} = 5.6^{+0.5}_{-0.5}$ and $z_{\rm all} = 5.5^{+0.5}_{-0.5}$. MMPZ estimates a lower limit of $z > 3.3$.

Source_17∗: A SPIRE-dropout with a clear IRAC and faint MIPS counterpart. This source is not detected (above 5σ) in *HST*. With IRAC and MIPS fluxes, MAGPHYS estimates $z = 3.2^{+0.2}_{-0.2}$. BAGPIPES estimates $z_{\rm opt/NIR} = 3.0^{+0.3}_{-0.3}$ and $z_{\rm all} = 2.4^{+0.3}_{-0.8}$. MMPZ estimates a lower limit of $z > 2.8$. The BAGPIPES $z_{\rm all}$ estimate is not consistent with MAGPHYS or MMPZ.

Source_20: A SPIRE-detected source with a strong detection in the MIPS and IRAC bands. Although the *HST* flux is $< 5\sigma$, since

we can see that it coincides with the position of the NIR and FIR source in the cut-outs, we choose to include the *HST* flux in our runs. We get a MAGPHYS photo-z estimate of $z = 1.9^{+0.1}_{-0.1}$. With BAGPIPES we estimate $z_{\rm opt/NIR} = 1.8^{+0.3}_{-0.7}$ and $z_{\rm all} = 1.7^{+0.2}_{-0.6}$. These estimates are inconsistent with the MMPZ estimate of $z = 2.7^{+0.4}_{-0.5}$. The position of the optical/NIR counterpart is 3.9 arcsec from the 850 μm source position, which is suggestive of lensing. Higher resolution sub-mm/mm observations are needed to confirm. We classify this source as potentially lensed.

Source_21∗: A SPIRE-dropout with a counterpart in MIPS and IRAC. MAGPHYS estimates a photo-z of $z = 2.4^{+0.2}_{-0.3}$. BAGPIPES estimates $z_{\rm opt/NIR} = 2.2^{+0.3}_{-0.3}$ and $z_{\rm all} = 1.3^{+0.4}_{-0.2}$. MMPZ estimates a lower limit of $z > 2.4$. The BAGPIPES $z_{\rm all}$ estimate does not agree with the rest of the photo-z estimates, so this source is categorized as having an inconsistent photo-z. There is a ~ 3.4 arcsec offset between the IRAC/MIPS source position and the 850 μm source position, which could suggest lensing. Higher resolution sub-mm/mm observations are needed to confirm whether or not lensing is taking place; meanwhile, we classify this source as potentially lensed.

Source_24∗: A SPIRE-dropout with a counterpart in the optical/NIR bands whose position is ~ 1 arcsec from the 850 μm source position. The *HST* flux for this source is $< 5\sigma$ but we include it since the *HST* source is clearly visible. MAGPHYS estimates a photo-z of $z = 3.2^{+0.2}_{-0.1}$. BAGPIPES estimates $z_{\rm opt/NIR} = 3.0^{+0.3}_{-0.3}$ and $z_{\rm all} = 2.8^{+0.2}_{-0.2}$. MMPZ estimates a lower limit of $z > 3.1$. The BAGPIPES $z_{\rm all}$ photo-z estimate is inconsistent with the MMPZ estimate. The offset between the optical/NIR counterpart and the 850 μm source may hint at a lensing situation. We label this source as a potential lens.

Source_25∗: A SPIRE-dropout with a clear MIPS and IRAC counterpart. The IRAC source breaks into multiple *HST* sources, so a robust optical cross-ID is not possible. With the NIR cross-ID, MAGPHYS estimates a photo-z of $z = 2.7^{+0.2}_{-0.2}$. From BAGPIPES, we get $z_{\rm opt/NIR} = 2.4^{+0.4}_{-0.4}$ and $z_{\rm all} = 2.0^{+0.3}_{-0.2}$. MMPZ estimates a lower limit of $z > 3.3$ meaning that the estimates are inconsistent. The four *HST* sources closest to the 850 μm contour have estimated optical photo-z's ranging $z \sim 0.5$–1.2, which is inconsistent with the above photo-z estimates. This source is unlikely to be a multiple, but we need spectroscopic observations to confirm this either way. We therefore classify this source as a potential multiple.

Source_26∗: A SPIRE-dropout with a potential *HST* counterpart located within the 850 μm cut-outs but ~ 2 arcsec from the 850 μm source position. Although the *HST* flux is $< 5\sigma$, we include it in our runs. This *HST* source has a faint IRAC counterpart matched via the catalogue. With MAGPHYS we estimate a photo-z of $z = 3.5^{+2.7}_{-1.4}$. BAGPIPES estimates $z_{\rm opt/NIR} = 6.7^{+0.6}_{-0.6}$ and $z_{\rm all} = 6.8^{+0.5}_{-0.5}$, while MMPZ estimates a lower limit of $z > 2.7$. The BAGPIPES $z_{\rm all}$ estimate is inconsistent with MAGPHYS. The offset between the *HST* source and the 850 μm position could suggest lensing, but higher resolution sub-mm/mm observations are needed to confirm this either way. We classify this source as potentially lensed.

Source_33: A bright SPIRE-detected source with a MIPS, IRAC, and *HST* counterpart. MAGPHYS estimates a photo-z of $z = 0.4^{+0.1}_{-0.1}$. Although this agrees with the BAGPIPES estimates of $z_{\rm opt/NIR} = 0.5^{+0.2}_{-0.3}$ and $z_{\rm all} = 0.3^{+0.1}_{-0.04}$, it is inconsistent with the MMPZ estimate of $z = 1.9^{+0.4}_{-0.4}$. We note that the MIPS source may be a blend of multiple IRAC sources, leading to the inconsistency between the photo-z estimates. For the IRAC sources above and below the 850 μm IRAC counterpart, we get a BAGPIPES photo-z of $z \sim 0.4$ and $z \sim 3.1$, respectively. This suggests that some IRAC sources may be physically associated. We classify this source as a potential multiple.

3.4.3 *Insufficient data*

Source_0∗: A source that is undetected in all SPIRE bands, making it a SPIRE-dropout. Despite the $> 4\sigma$ detection at 850 μm, this source has no counterparts at optical or NIR wavelengths. There are two faint sources visible within the 850 μm contour in the *HST* image, but with no other optical/NIR counterparts available, there are insufficient data to make photo-z estimates. MMPZ estimates a photo-z of $z \sim 11.4$ but given that this source has unphysical negative SPIRE flux constraints, the MMPZ is unreliable. We try MMPZ again using the SPIRE confusion noise to calculate the 3σ SPIRE upper limits, and obtain a photo-z estimate of $z = 2.8^{+0.6}_{-0.6}$, suggesting an intermediate redshift.

Source_2∗: A SPIRE-dropout with no MIPS counterpart, but which potentially has two faint IRAC counterparts located within the 850 μm contour, which are not clearly visible in the cut-outs. The IRAC sources are located within 1.5 arcsec of each other, and each also has a *HST* flux associated with it. The BAGPIPES estimates for these IRAC sources are $z = 1.2^{+2.7}_{-0.8}$ and $z = 1.2^{+0.9}_{-0.7}$, suggesting they are physically associated. The 850 μm is likely a blend of these two IRAC sources but without a robust match, this source is categorized as having insufficient data. We also classify this source as a potential multiple in IRAC bands; spectroscopic data are required to confirm this. MMPZ estimates a photo-z of $z = 3.1^{+3.1}_{-1.4}$, which, we note, is consistent with the BAGPIPES estimates of the two IRAC sources. However, we reiterate that we do not have a singular, robust optical/NIR counterpart.

Source_3∗: A SPIRE-dropout with a faint MIPS counterpart. In the IRAC bands, at least three sources are visible within the 850 μm beam, all of which have one or more *HST* counterparts. With BAGPIPES, we estimate the photo-z's for the three IRAC sources within the 850 μm beam (starting with the bottom source and going clockwise) of $z = 1.0^{+0.8}_{-0.4}$, $0.8^{+0.2}_{-0.2}$, and $0.7^{+0.5}_{-0.2}$, respectively. These IRAC sources may be a physically associated multiple, blended together in MIPS but identifying any singular IRAC source as the sole contributor to the FIR source is not possible without precise coordinates from higher resolution data. With only the MIPS source as a definite cross-ID, we cannot make any robust optical/NIR photo-z estimates. Therefore, this source is classified as having insufficient data and as being a potential multiple. MMPZ estimates a photo-z of $z = 5.5^{+4.0}_{-1.5}$.

Source_5∗: A SPIRE-dropout with a faint MIPS counterpart. In the IRAC bands, three sources are visible within the 850 μm beam, some of which are made up of multiple *HST* sources. The three IRAC sources (starting with the top-most source and going clockwise) have BAGPIPES estimates of $z = 2.9^{+1.9}_{-2.3}$, $1.5^{+1.9}_{-0.8}$, and $1.9^{+2.4}_{-0.8}$, respectively, suggesting the latter two may be physically associated. Without precise coordinates, we cannot identify the assumed singular IRAC match. With only a MIPS flux available, we cannot make any robust photo-z estimates with BAGPIPES. We classify this source as a likely multiple. MMPZ estimates a photo-z of $z = 3.3^{+0.7}_{-0.6}$, which is consistent with the estimates of the IRAC sources, but we cannot be certain, without spectroscopic data, which, if any, is the correct counterpart.

Source_6: While having a detection with SPIRE, we find no clear counterpart at shorter wavelengths. The nearest MIPS source to the 850 μm position has a clear IRAC counterpart that de-blends into multiple potential counterparts in *HST*. However,

this MIPS source is offset from the 850 μm position and contours by > 7 arcsec, making it an unlikely cross-ID. Therefore, the 850 μm source has no counterparts in the optical/NIR. With MMPZ, we estimate a redshift based on FIR photometry of $z = 2.2^{+2.2}_{-1.7}$ but with no shorter wavelength photometry available, this source remains essentially unconstrained.

Source_8: A SPIRE-detected source with a faint MIPS counterpart that corresponds to a blend of IRAC and *HST* sources. The MIPS source appears to be a blend of at least three *HST* sources that lie at an estimated photo-z of $z = 2.9^{+0.8}_{-1.3}$, $z = 2.0^{+2.0}_{-1.4}$, and $z = 1.4^{+1.5}_{-0.8}$, respectively, starting with the top-most *HST* source to the bottom-most source within the central 850 μm contour. Without a clear IRAC/*HST* match to the MIPS source, we cannot make any further optical/NIR photo-z estimates. Spectroscopic observations are needed to confirm whether the optical sources are physically associated. We class this as a potential multiple source. MMPZ estimates a photo-z of $z = 3.2^{+1.2}_{-1.1}$.

Source_9∗: A SPIRE-dropout with no MIPS counterpart or IRAC counterpart. There is another bright IRAC source, with an MIPS counterpart, just outside the 850 μm contours. There are also two faint IRAC sources nearby but still outside the 850 μm contours. None of these sources correspond clearly to the 850 μm source so it is difficult to make a robust cross-ID. MMPZ estimates a photo-z of $z = 6.8^{+4.8}_{-1.9}$, using the negative SPIRE constraints. With the 3σ SPIRE upper limits, MMPZ estimates $z = 2.2^{+0.5}_{-0.5}$, which suggests an intermediate redshift compared to the initial high-z estimate. Without a robust counterpart match, we cannot make further constraints to the redshift.

Source_11: No clear MIPS or IRAC catalogue match. The 850 μm source position is in the middle of multiple optical/NIR sources, one of which corresponds to the SPIRE contours, which appear to be offset from the 850 μm source by ∼ 6 arcsec. With this large offset, it is unclear whether this particular MIPS source is the counterpart to the 850 μm source. The three IRAC sources visible within the 850 μm beam have optical/NIR photo-z estimates of $z = 1.0^{+1.0}_{-0.3}$, $z = 1.2^{+0.9}_{-0.6}$, and $z = 0.6^{+1.6}_{-0.5}$, respectively, starting with the top-right IRAC source (corresponding to the SPIRE contour) and going clockwise, suggesting that these sources may be physically associated. The multiple IRAC/*HST* sources add to the difficulty of identifying a robust counterpart and spectroscopic data are required to confirm whether they are physically associated. We classify this source as 'Insufficient Data' and as a likely multiple. MMPZ estimates a photo-z of $z = 2.4^{+2.3}_{-1.9}$.

Source_12: Multiple candidate shorter wavelength counterparts. There is only one MIPS source within the 850 μm beam, but multiple IRAC/*HST* sources. The two brighter IRAC sources (right and left) within the 850 μm contour are estimated to reside at $z = 2.2^{+2.0}_{-0.9}$ and $z = 0.9^{+0.8}_{-0.3}$, respectively, suggesting that they are unlikely to be physically associated. The IRAC sources themselves appear to be blends of multiple *HST* sources, but without a specific IRAC counterpart, we do not have enough photometry data to estimate their photo-z. We class this source as having insufficient data and as a potential multiple at optical/NIR bands. MMPZ estimates a photo-z of $z = 3.3^{+0.7}_{-0.6}$.

Source_18∗: A SPIRE-dropout with multiple IRAC and *HST* sources visible within the 850 μm beam but none corresponding to the 850 μm position. The three bright IRAC sources within the 850 μm beam have optical/NIR photo-z estimates of $z = 0.8^{+0.4}_{-0.3}$, $1.1^{+1.2}_{-0.5}$, and $0.9^{+1.0}_{-0.3}$, respectively, starting with the top source and going clockwise. Without a clear counterpart, this source is classified as having insufficient data. We additionally class this source as a potential multiple, but spectroscopic data are required to confirm this. MMPZ estimates a photo-z of $z = 4.2^{+3.9}_{-1.3}$.

Source_19: While this 850 μm source has a clear detection in the SPIRE bands, the FIR source is resolved into at least two MIPS sources, which themselves are resolved into multiple IRAC sources. The two MIPS sources (top right and bottom left) have optical/NIR photo-z estimates of $z = 0.6^{+0.6}_{-0.2}$ and $z = 1.8^{+0.7}_{-1.1}$, respectively. Although they may not be physically associated, they make it difficult to accurately identify the optical/NIR counterpart of the FIR source. Without a robust optical counterpart available, there is not enough data to constrain the photo-z. Spectroscopic data are needed to determine the true redshifts of the multiple sources. MMPZ estimates a photo-z of $z = 2.3^{+0.6}_{-0.6}$.

Source_22∗: A SPIRE-dropout with multiple MIPS/IRAC sources visible within the 850 μm beam. Without a clear optical/NIR counterpart, there are not enough data to constrain the photo-z. Of the various *HST* sources visible within the 850 μm contour, we identify six of them in the IRAC catalogue and estimate photo-z's ranging $z \sim 0.6$–1.5, suggesting that some of these sources may be physically associated. This source therefore has a potentially high multiplicity, but we need spec-z to confirm this. MMPZ estimates a photo-z of $z = 4.4^{+3.9}_{-1.5}$.

Source_23: This source may have a bright IRAC counterpart; however, this IRAC source, located on the edge of the 850 μm contour, is resolved into multiple *HST* sources that are all located outside of the 850 μm contour. No other optical sources coincide with the 850 μm position. MMPZ estimates a photo-z of $z = 2.0^{+0.4}_{-0.4}$.

Source_27∗: A SPIRE-dropout with no counterpart in MIPS. Multiple IRAC/*HST* sources visible within the 850 μm beam, but no obvious match. Seven IRAC catalogue sources are located within the 850 μm beam but are undetected in many of the optical/NIR bands. These sources reside at photo-z's ranging $1 < z < 2.4$. Without a robust cross-ID we cannot make any further photo-z estimates. We classify this source as a potential multiple; several of these optical sources may be physically associated, and we need spec-z to confirm this. MMPZ estimates a photo-z of $z = 3^{+3.9}_{-1.6}$.

Source_28: Has a clear MIPS counterpart that resolves into two IRAC sources within the 850 μm contour, both of which are in the IRAC catalogue. For these two sources, BAGPIPES estimates an optical/NIR photo-z of $z \sim 2.3$ and 0.9, respectively, for the upper and lower source. These sources do not appear to be physically associated but their close proximity in the cut-outs makes an accurate IRAC/*HST* cross-ID difficult. We classify this source as 'Insufficient Data'. MMPZ estimates a photo-z of $z = 3.3^{+0.7}_{-0.6}$.

Source_29: We identify the optical object as a star, with confirmation from the *Gaia* archive. Using the available parameters of the star, we conclude that it is unlikely to be physically associated with the FIR source and is most likely a chance alignment (see Section 3.5). As such, we are left with only the FIR/submm fluxes, leaving the available photometry of this source insufficient for a robust photo-z estimate.

Source_31∗: A faint *HST* source is visible 0.5 arcsec from the 850 μm position. The closest catalogue match to this source is 0.1 arcsec from the *HST* source in the image. However, the three IRAC band fluxes that are available in the catalogue are < 5σ, which we classify as non-detections, leaving only the faint *HST* flux in the optical/NIR regime. Without more optical data available, there are insufficient data to constrain this source. The small offset of the faint *HST* source could be suggest lensing, but we

require higher resolution submm/mm data to confirm this. We classify this as potentially lensed. MMPZ estimates a photo-z of $z = 3.8^{+4.3}_{-1.5}$.

Source_32∗: There are four faint IRAC sources, with a maximum distance of 4 arcsec, around the 850 μm position. All but one of these IRAC sources have an *HST* counterpart, with estimated photo-z's ranging $z \sim 1.2$–2.5. With no MIPS counterpart and multiple IRAC candidates, we are unable to make a robust optical/NIR photo-z estimate. This source is a potential multiple. MMPZ estimates a photo-z of $z = 2.8^{+0.7}_{-0.6}$.

Source_34: No clear IRAC or MIPS counterpart. There are two faint *HST* sources visible within the 850 μm contour, one of which appears in the IRAC catalogue, but neither has a visible IRAC counterpart in the cut-outs. The catalogue source has no optical detections. With detections in only two IRAC bands, there is not enough data to constrain this source. MMPZ estimates a photo-z of $z = 2.7^{+0.6}_{-0.6}$.

Source_35∗: A SPIRE-dropout with no counterpart in MIPS. The 850 μm coordinates of this source are outside the dimensions of our *HST* image. The IRAC cut-out shows a bright object spreading over almost the entire 850 μm beam, which corresponds to at least three IRAC catalogue sources. This bright object in IRAC is an offset bright source leaking onto the 850 μm position. MMPZ estimates a photo-z of $z \sim 11.4$, but this is unreliable since the SPIRE constraints for this source are all negative. Using the 3σ SPIRE upper limits, MMPZ estimates $z = 2.7^{+1.1}_{-1.1}$, which suggests an intermediate/high redshift. Without any other optical/NIR data available, we cannot reliably determine a counterpart to the 850 μm source or further constrain the redshift of this source.

Out of a total of 36 Deep Region sources, three sources are classified as having a consistent photo-z, 13 are classified as having an inconsistent photo-z between the various methods, and the remaining 20 are classified as having insufficient data. More than 50 per cent of the sources in the 'Inconsistent photo-z' and 'Insufficient Data' groups are SPIRE-dropouts, highlighting the difficulty in constraining this type of source. Without a SPIRE detection, identifying optical/NIR counterparts is difficult when any optical/NIR sources that may be visible within the 850 μm beam are blended together at submm wavelengths; for example, see Fig. 5 for cut-outs of Sources 3*, 5*, 25*, and 33. Even with the 850 μm position, a robust cross-ID is not possible. In other cases, the high-redshift nature of the SPIRE-dropouts may mean that sometimes an optical/NIR source is not present, leading to insufficient data available to make a photo-z estimate; for example, see Fig. 5 for cut-outs of Sources 0*, 6, and 34.

Despite the difficulties in making a cross-ID, we are able to obtain consistent photo-z estimates for three of our sources; see Fig. 5 for cut-outs of Sources 14, 16, and 30. For these consistent sources, there is usually one clearly visible counterpart that coincides with both the 850 μm source and the SPIRE source. The consistent photo-z between MAGPHYS, BAGPIPES, and MMPZ is another indication that the cross-ID is likely to be correct, as the optical/NIR source and the FIR source are suggested to be physically associated.

When assigning counterparts to our SDF sources, we also determine whether there is a possibility of multiplicity or lensing. We classify nine sources from our sample as potentially lensed due to an offset between the optical/NIR source and 850 μm source position (marked with 'PL' in Table 4). We do not find any evidence of lensing in the images; hence, we require higher resolution submm/mm data to accurately identify any true cases of lensing, which would affect the estimated physical properties that we calculate in Section 4. A total of 15 sources are classified as potential multiples (marked with 'PM' in Table 4). We classify these sources as multiple in terms of the contribution of optical/NIR sources to the SPIRE/850 μm flux.

Table 3. Stacked SPIRE and SCUBA-2 fluxes of the 20 SPIRE-dropout sources along with the corresponding standard error.

SPIRE band	Stacked flux [mJy]
250 μm	5.6 ± 1.4
350 μm	7.9 ± 1.6
500 μm	8.5 ± 1.6
850 μm	4.6 ± 0.2

We also take advantage of the higher than expected fraction of SPIRE-dropouts in our sample and calculate their stacked FIR fluxes. Stacking is a commonly used technique that allows one to statistically detect the average signal of a population of sources that are individually too faint to be detected above the noise in a given data set (e.g. H. Dole et al. 2006; M. P. Viero et al. 2013). This method is particularly powerful in confusion-limited regimes such as FIR and submm wavelengths. In this work, we perform stacking of the *Herschel*-SPIRE and SCUBA-2 850 μm fluxes of our SPIRE-dropouts, which are individually undetected in SPIRE, to estimate their average FIR/submm fluxes. We use the SPIRE and 850 μm flux densities and errors of each SPIRE-dropout as listed in Table 4. The SPIRE fluxes in each band are simply averaged to calculate the stacked mean flux, and the stacked error is calculated using equation (2).

$$\sigma = \sqrt{\frac{1}{N}\sum_{i=1}^{N}(S_i - \bar{S})^2}, \tag{2}$$

where N is the number of SPIRE-dropouts, $\bar{S}$ is the average flux for a SPIRE band, and S_i is the flux of the ith source.

For the 850 μm stacked flux, since we are taking the individual errors of each dropout into account, we use an inverse-variance weighted method as shown in equation (3).

$$S_{\rm stack} = \frac{\sum_{i=1}^{N} w_i S_i}{\sum_{i=1}^{N} w_i}, \quad \sigma_{\rm w} = \sqrt{\frac{1}{\sum_{i=1}^{N} w_i}}, \quad w_i = \frac{1}{\sigma_i^2}, \tag{3}$$

where σ_i is the 850 μm flux error of the ith source, w_i is the weight of the ith source, S_i is the 850 μm flux density of the ith source, $S_{\rm stack}$ is the stacked 850 μm flux, and σ_w is the associated 850 μm stacked flux error.

Table 3 shows the stacked fluxes for the SPIRE-dropouts in the SPIRE and SCUBA-2 850 μm bands, along with the corresponding standard error. These represent the average FIR fluxes of the SPIRE-dropouts in the Deep Region and show that the average fluxes are detected in all bands. MMPZ estimates a photo-z of $z = 4.0^{+0.1}_{-0.6}$ with these stacked fluxes.

3.5 Source_29

We briefly discuss the SCUBA-2 850 μm-detected Source_29 that is spatially coincident with a stellar object visible in optical imaging. To investigate the nature of this optical counterpart, we searched archival data sets and found a match in the WISE catalogue (R. M. Cutri et al. 2013) within ~ 1 arcsec of the 850 μm source position. This source is also cross-identified in SDSS and 2MASS, and appears in the GAIA DR3 catalogue (Gaia Collaboration et al. 2023), which provides parallax, proper motion, and

astrophysical parameters. The object has an effective temperature of $T_{\rm eff} = 4439$ K, consistent with a K-type main-sequence star located at a distance of ~ 1 kpc. Our own optical spectroscopy, obtained with the Liverpool Telescope (Project ID PQ24B03; PI: D. L. Clements), supports this stellar classification.

Using the FIR photometry (SPIRE and SCUBA-2), we estimate a photometric redshift of $z \approx 3.0$ for Source_29 with MMPZ. No archival spectroscopic redshift is available for the FIR source. The coincidence of the FIR and optical positions raises the question of whether the FIR emission is physically associated with the star, or whether this is simply a chance alignment between a foreground stellar object and a background dusty galaxy.

The simplest and most probable explanation is a chance alignment, in which the optical star lies along the line of sight to a high-z FIR source. This is supported by the high photo-z estimate and the lack of any evident connection between the stellar properties and the submm emission. However, if the FIR emission were associated with the star, it could imply the presence of a substantial circumstellar dust reservoir, such as a debris disc, or a more exotic stellar environment.

The FIR and optical positions agree to within ~ 1 arcsec, comparable to the positional uncertainties of the SPIRE and SCUBA-2 instruments, meaning that this spatial alignment is not conclusive. To resolve the ambiguity, high-resolution interferometric observations are required. Ongoing SMA observations will provide sub-arcsecond astrometry of the FIR source. If the FIR emission is spatially offset from the star, this would confirm its extragalactic origin. Conversely, if the FIR emission is co-spatial with the star, it would mark the object as a highly unusual and potentially important case for further investigation. Using the parameters from *Gaia*, we estimate the stellar luminosity of the optical source associated with Source_29 to be $L_\star \approx 0.17\,{\rm L}_\odot$, consistent with expectations for a K-type main-sequence star (e.g. T. S. Boyajian et al. 2012). We then compare this to the infrared luminosity (integrated over 8–1000 μm) of the FIR source, derived from SPIRE and SCUBA-2 photometry and SED fitting, and assuming it is physically associated with the optical star, which yields $L_{\rm IR} \approx 67\,{\rm L}_\odot$. This results in an infrared excess ratio of $L_{\rm IR}/L_\star \approx 392$, many orders of magnitude higher than what is physically plausible for any known stellar object, including stars with debris discs or circumstellar dust envelopes. For comparison, typical IR excesses for stars with circumstellar material lie in the range $L_{\rm IR}/L_\star \sim 10^{-5}$–$10^{-2}\,{\rm L}_\odot$ (e.g. M. C. Wyatt 2008). This extremely high excess therefore provides compelling evidence that the FIR emission is not associated with the stellar source, but rather originates from a background DSFG at high-z, as also supported by the FIR-derived photo-z estimate of $z \approx 3$. We thus conclude that this is most likely a chance line-of-sight alignment between a foreground star and a high-z extragalactic FIR source.

3.6 Redshift distribution

Using the photo-z estimates from Section 3.4, we investigate the redshift distribution of our SDF sources and compare with various results from the literature. For this analysis, we plot the distributions of the SPIRE detected sources and the SPIRE-dropouts separately. To construct our redshift distribtuion, for the SPIRE-detected sources with a consistent photo-z, we use their BAGPIPES opt/NIR photo-z estimate as stated in Table 4. For the SPIRE-detected sources with inconsistent photo-z or with insufficient data, we use their MMPZ estimate from Table 4. For the SPIRE-dropouts (sources marked with an asterisk next to their name in Table 4), we use their MMPZ estimate. Fig. 8 shows the redshift distribution of these two source populations.

The redshift distributions of sources from the literature have median photo-z's ranging from $z \sim 1.7$–3.1 with a possible tail extending out to $z \sim 6$. Our SPIRE-detected sample has a median photo-z of 2.3 with an interquartile range of 0.8, in agreement with the quoted literature range. We also see a high-z tail at $z > 5$, which represents the estimated photo-z of the dropouts. While these redshift estimates are not confirmed, the distribution visually highlights the high-z nature of the dropouts compared to the SPIRE-detected sample.

4 PHYSICAL PROPERTIES OF SDF GALAXIES

4.1 FIR SED fitting

To extract physical properties for our SDF sources, we take the SPIRE and SCUBA-2 850 μm photometry, and, following the literature convention (C. M. Casey et al. 2012, 2014; B. Magnelli et al. 2012; J. Greenslade et al. 2020), fit them to a single temperature modified blackbody function of the form

$$S_\nu \propto [1 - \exp(-\tau_\nu)]B_\nu({\rm T}), \tag{4}$$

where S_ν is the observed flux density in mJy at frequency ν (such that $\nu = \nu_{\rm obs}(1+z)$) and τ_ν is the optical depth of the dust defined as $\tau_\nu = (\nu/\nu_0)^\beta$, where ν_0 is the frequency at which $\tau_\nu = 1$, and β is the dust emissivity index. $B_\nu(T)$ is the Planck function for a given temperature T, defined as

$$B_\nu(T) = \frac{2h\nu^3}{c^2}\frac{1}{\exp\left(\frac{h\nu}{k_{\rm B}T}\right) - 1}. \tag{5}$$

To perform our fit, we use the `emcee` [4] package (D. Foreman-Mackey et al. 2013), a python-based Affine Invariant Markov Chain Monte Carlo (MCMC) Ensemble Sampler. Since we are only fitting four photometric points, we reduce the number of degrees of freedom by fixing $c/\nu_0 = 200$ μm following A. Conley et al. (2011) and C. M. Casey et al. (2012). First, we consider the case of the SPIRE-detected sample. The redshifts used for the SED fitting of these sources are taken from Table 4. We fix the redshift for each source to the BAGPIPES opt/NIR estimate if the source is grouped under 'Consistent photo-z', and to the MMPZ estimate if the source is grouped under 'Inconsistent/Insufficient photo-z'. Table 5 states the final redshift used for the SED fitting of each SPIRE-detected source. We are then left with three parameters for our fit: the dust temperature $T_{\rm dust}$, the dust emissivity index β, and the normalization factor A. We use the SPIRE and SCUBA-2 fluxes as stated in Table 4, but for all sources, we use the SPIRE confusion noise as the SPIRE flux errors (i.e. 5.8, 6.3, 6.8 mJy at 250, 350, 500 μm, respectively) since this is the dominant source of noise. We use the `emcee` Ensemble Sampler with the following uninformative priors for our parameters: $10\,{\rm K} < T_{\rm dust} < 80\,{\rm K}$, $1 < \beta < 3$, and $-20 < \log_{10}(A) < -10$. We estimate initial best-fitting parameters for each source through a maximum likelihood estimation, which we then visually inspect to ensure a reasonable fit. We then initialize 250 walkers in a small Gaussian ball around our initial best-fitting parameters and allow 50 000 steps in our MCMC chains. Following the `emcee` documentation and D. Foreman-Mackey et al. (2013), we use the

[4] https://emcee.readthedocs.io/en/stable/

Table 4. Sources with a robust cross-ID whose photo-z estimates from MAGPHYS, BAGPIPES, and MMPZ are all consistent within the respective uncertainties are grouped as 'Consistent photo-z'. If the four photo-z estimates are not all consistent within the respective uncertainties, then they are grouped under 'Inconsistent photo-z'. The remaining sources, for which a robust optical/NIR cross-ID is not possible, are grouped under 'Insufficient Data', where we only have a photo-z estimate from MMPZ. For MAGPHYS, we state the median of the best-fitting model's PDF, and the error reflecting the 16–84th percentiles of this distribution; this is the redshift used for comparison. In the square brackets, we state the best-fitting MAGPHYS redshift. For each BAGPIPES estimate, we state the median value and the error reflecting the 16–84th percentile of the BAGPIPES posterior. For the MMPZ photo-z estimate, we state the mode of the $P(z)$ distribution and the upper/lower bound of the 68 per cent minimum credible interval. For SPIRE-dropouts we state the mode of the $P(z)$ distribution as a MMPZ lower limit. Sources marked with an asterisk are SPIRE-dropouts. For sources that have map-extracted SPIRE constraints, we set the flux error as the SPIRE confusion noise. Some SPIRE flux constraints are negative, since those sources are SPIRE-dropouts. PM = Potentially multiple. PL = Potentially lensed.

ID	RA [deg]	Dec. [deg]	S_{250} [mJy]	S_{350} [mJy]	S_{500} [mJy]	S_{850} [mJy]	SNR_{850}	MAGPHYS z_{all}	BAGPIPES $z_{\mathrm{opt/NIR}}$	BAGPIPES z_{all}	MMPZ $z_{\mathrm{FIR/submm}}$	Notes
Consistent photo-z												
Source_14	265.0643	68.9842	48.10 ± 0.21	35.49 ± 0.20	17.66 ± 0.24	5.15 ± 1.19	5.5	$0.9^{+0.1}_{-0.1}$ [1.0]	$1.0^{+0.2}_{-0.1}$	$0.9^{+0.1}_{-0.1}$	$1.4^{+0.2}_{-0.4}$	PM
Source_16	265.2844	68.9906	23.56 ± 5.8	17.73 ± 6.3	15.76 ± 6.8	3.51 ± 1.18	4.1	$2.2^{+0.2}_{-0.2}$ [2.2]	$1.9^{+0.5}_{-0.6}$	$2.0^{+0.2}_{-0.1}$	$1.8^{+0.4}_{-0.5}$	PL
Source_30	265.2076	69.0841	19.13 ± 5.8	16.25 ± 6.3	14.49 ± 6.8	4.72 ± 1.27	4.8	$1.4^{+0.3}_{-0.2}$ [1.4]	$1.2^{+0.4}_{-0.3}$	$1.2^{+0.2}_{-0.2}$	$2.3^{+1.8}_{-1.5}$	PL
Inconsistent photo-z												
Source_1*	264.9715	68.9308	2.13 ± 5.8	3.64 ± 6.3	8.24 ± 6.8	4.36 ± 1.18	4.8	$3.2^{+1.0}_{-0.6}$ [2.9]	$3.0^{+0.4}_{-0.4}$	$2.5^{+0.4}_{-0.4}$	> 4.5	PM
Source_4	264.7241	68.9439	35.04 ± 0.32	29.05 ± 0.30	19.25 ± 0.36	5.48 ± 1.55	4.7	$3.4^{+0.1}_{-0.2}$ [3.2]	$3.1^{+0.3}_{-0.4}$	$2.3^{+0.3}_{-0.4}$	$2.3^{+0.2}_{-0.3}$	PM
Source_7*	264.9374	68.9508	0.98 ± 5.8	2.08 ± 6.3	1.97 ± 6.8	6.35 ± 1.22	6.5	$3.6^{+2.0}_{-0.9}$ [5.4]	$5.3^{+0.5}_{-0.5}$	$5.3^{+0.5}_{-0.5}$	> 6.5	PL
Source_10*	265.1417	68.9663	8.92 ± 5.8	10.40 ± 6.3	6.93 ± 6.8	3.59 ± 1.15	4.3	$1.8^{+0.2}_{-0.1}$ [1.8]	$1.6^{+0.4}_{-0.5}$	$1.1^{+0.3}_{-0.2}$	> 2.7	PL
Source_13	264.9156	68.9808	16.28 ± 5.8	30.80 ± 6.3	31.50 ± 6.8	4.17 ± 1.35	4.2	$2.7^{+0.7}_{-0.5}$ [1.2]	$0.8^{+0.5}_{-0.3}$	$1.5^{+0.6}_{-0.5}$	$2.3^{+1.8}_{-1.5}$	—
Source_15*	264.9590	68.9853	2.50 ± 5.8	5.71 ± 6.3	13.41 ± 6.8	3.50 ± 1.14	4.2	$3.6^{+1.0}_{-0.8}$ [5.7]	$5.6^{+0.5}_{-0.5}$	$5.5^{+0.5}_{-0.5}$	> 3.3	—
Source_17*	265.2100	68.9907	11.79 ± 5.8	17.48 ± 6.3	14.56 ± 6.8	5.15 ± 1.19	5.5	$3.2^{+0.2}_{-0.2}$ [2.9]	$3.0^{+0.3}_{-0.3}$	$2.4^{+0.3}_{-0.8}$	> 2.8	—
Source_20	265.0954	69.0042	16.71 ± 5.8	15.35 ± 6.3	9.13 ± 6.8	5.10 ± 1.19	5.5	$1.9^{+0.1}_{-0.1}$ [1.9]	$1.8^{+0.3}_{-0.7}$	$1.7^{+0.2}_{-0.6}$	$2.7^{+0.4}_{-0.5}$	PL
Source_21*	265.1357	69.0130	16.20 ± 5.8	20.55 ± 6.3	15.62 ± 6.8	4.64 ± 1.17	5.1	$2.4^{+0.2}_{-0.3}$ [2.4]	$2.2^{+0.3}_{-0.3}$	$1.3^{+0.4}_{-0.2}$	> 2.4	PL
Source_24*	265.2476	69.0318	15.17 ± 5.8	20.19 ± 6.3	26.83 ± 6.8	7.79 ± 1.30	7.5	$3.2^{+0.2}_{-0.1}$ [3.2]	$3.0^{+0.3}_{-0.3}$	$2.8^{+0.2}_{-0.2}$	> 3.1	PL
Source_25*	264.8532	69.0330	3.93 ± 5.8	6.77 ± 6.3	6.42 ± 6.8	3.48 ± 1.17	4.1	$2.7^{+0.2}_{-0.2}$ [2.6]	$2.4^{+0.4}_{-0.4}$	$2.0^{+0.3}_{-0.2}$	> 3.3	PM
Source_26*	264.8003	69.0484	12.02 ± 5.8	11.06 ± 6.3	5.06 ± 6.8	4.24 ± 1.27	4.5	$3.5^{+2.7}_{-1.4}$ [7.0]	$6.7^{+0.6}_{-0.6}$	$6.8^{+0.5}_{-0.5}$	> 2.7	PL
Source_33	264.9679	69.0997	23.42 ± 0.27	21.86 ± 0.26	13.19 ± 0.32	7.44 ± 1.38	6.8	$0.4^{+0.1}_{-0.1}$ [0.4]	$0.5^{+0.2}_{-0.3}$	$0.3^{+0.1}_{-0.04}$	$1.9^{+0.4}_{-0.4}$	PM

ID	RA [deg]	Dec. [deg]	S_{250} [mJy]	S_{350} [mJy]	S_{500} [mJy]	S_{850} [mJy]	SNR_{850}	MMPZ z	Notes
Insufficient Data									
Source_0*	265.1444	68.8808	-5.28 ± 5.8	-6.47 ± 6.3	-5.45 ± 6.8	4.76 ± 1.49	4.3	> 11.4	—
Source_2*	264.9529	68.9408	8.05 ± 5.8	8.97 ± 6.3	11.19 ± 6.8	3.90 ± 1.16	4.5	> 3.1	PM
Source_3*	264.8632	68.9441	1.29 ± 5.8	1.81 ± 6.3	3.00 ± 6.8	4.01 ± 1.21	4.4	> 5.5	PM
Source_5*	265.1447	68.9463	9.67 ± 5.8	12.97 ± 6.3	10.15 ± 6.8	5.30 ± 1.20	5.6	> 3.3	PM
Source_6	265.0488	68.9508	14.87 ± 5.8	20.03 ± 6.3	18.90 ± 6.8	3.74 ± 1.15	4.4	$2.2^{+2.2}_{-1.7}$	—

Table 4 – *continued*

ID	RA [deg]	Dec. [deg]	S_{250} [mJy]	S_{350} [mJy]	S_{500} [mJy]	S_{850} [mJy]	SNR_{850}	MMPZ z	Notes
Source_8	265.0890	68.9519	12.46 ± 5.8	19.24 ± 6.3	22.17 ± 6.8	7.64 ± 1.27	7.6	$3.2^{+1.2}_{-1.1}$	PM
Source_9*	264.9034	68.9563	-2.66 ± 5.8	-0.03 ± 6.3	-1.39 ± 6.8	3.63 ± 1.15	4.3	> 6.8	—
Source_11	265.3770	68.9683	13.15 ± 5.8	23.39 ± 6.3	21.01 ± 6.8	4.12 ± 1.37	4.1	$2.4^{+2.3}_{-1.9}$	PM
Source_12	264.9311	68.9808	35.33 ± 0.21	45.80 ± 0.20	40.52 ± 0.25	4.51 ± 1.16	5.0	$3.3^{+0.7}_{-0.6}$	PM
Source_18*	264.8660	68.9930	7.54 ± 5.8	5.45 ± 6.3	3.23 ± 6.8	5.15 ± 1.19	5.5	> 4.2	PM
Source_19	264.9651	68.9941	22.77 ± 5.8	25.60 ± 6.3	22.56 ± 6.8	5.69 ± 1.20	6.0	$2.3^{+0.6}_{-0.6}$	—
Source_22*	265.0178	69.0242	3.79 ± 5.8	5.48 ± 6.3	7.02 ± 6.8	5.54 ± 1.20	5.8	> 4.4	PM
Source_23	264.9868	69.0242	18.28 ± 5.8	20.37 ± 6.3	13.24 ± 6.8	3.73 ± 1.15	4.4	$2.0^{+0.4}_{-0.4}$	—
Source_27*	265.2478	69.0596	5.50 ± 5.8	12.20 ± 6.3	12.96 ± 6.8	3.51 ± 1.21	4.0	> 3.0	PM
Source_28	265.0240	69.0719	21.32 ± 0.24	27.31 ± 0.23	25.22 ± 0.28	4.38 ± 1.19	4.8	$3.3^{+0.7}_{-0.6}$	—
Source_29	264.8497	69.0796	32.61 ± 0.28	45.02 ± 0.27	33.57 ± 0.32	8.18 ± 1.42	7.2	$3.0^{+0.7}_{-0.6}$	—
Source_31*	264.9212	69.09301	2.28 ± 5.8	8.10 ± 6.3	12.51 ± 6.8	3.92 ± 1.28	4.2	> 3.8	PL
Source_32*	264.8808	69.09520	12.90 ± 5.8	16.65 ± 6.3	17.63 ± 6.8	5.40 ± 1.37	5.1	> 2.8	PM
Source_34	265.0769	69.10304	12.39 ± 5.8	19.58 ± 6.3	20.40 ± 6.8	5.27 ± 1.30	5.2	$2.7^{+0.6}_{-0.6}$	—
Source_35*	264.9928	69.1319	-4.81 ± 5.8	-4.30 ± 6.3	-0.39 ± 6.8	4.29 ± 1.48	4.0	> 11.4	—

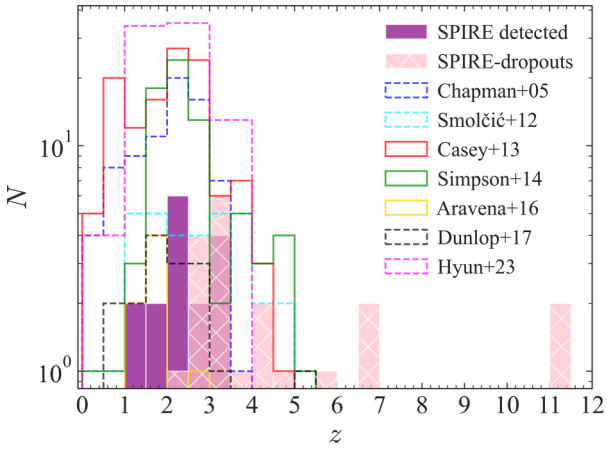

Figure 8. Redshift distribution of SPIRE detected sources and SPIRE-dropouts in our SDF sample. The SPIRE detected sample has a median photo-z of 2.3 with an interquartile range of 0.8. The SPIRE-dropouts have a median photo-z of 3.3 with an interquartile range of 1.8. Literature results are shown from the following: C. M. Casey et al. 2013; S. C. Chapman et al. 2005; Aravena et al. 2016; Smolčić et al. 2012; Simpson et al. 2014; J. Dunlop et al. 2017; Hyun et al. 2023.

Table 5. Characteristic dust temperatures values, along with derived dust masses, FIR luminosities and corresponding SFRs based on the integrated FIR/submm photometry for our SPIRE-detected Deep Region sources. The corresponding redshift chosen to be used in the fit of each source is also shown. Source marked with a star (⋆) are grouped under 'Inconsistent photo-z', while sources marked with a dagger (†) are grouped under 'Insufficient Data'. For these two source categories, we use their MMPZ redshift estimate in the FIR SED fitting procedure. The rest of the sources have a 'Consistent photo-z' so we use their BAGPIPES (opt/NIR) estimate. The last two rows show the average properties of the stacked SPIRE-dropouts; z is a free parameter ($z_{\rm free}$) for the first row of SPIRE-dropout results and is fixed for the second row ($z_{\rm fix}$). PM = Potentially multiple. PL = Potentially lensed.

ID	$T_{\rm dust}$ [K]	$\log_{10}(M_{\rm dust}/{\rm M}_\odot)$	$\log_{10}(L_{\rm FIR}/{\rm L}_\odot)$	$\rm SFR_{obsc}$ [$\rm M_\odot\ yr^{-1}$]	z	Notes
Source_4⋆	39.7^{+10}_{-8}	$8.43^{+0.16}_{-0.15}$	$14.4^{+0.5}_{-0.6}$	27000^{+64000}_{-20000}	$2.3^{+0.2}_{-0.3}$	PM
Source_6†	29.9^{+9}_{-6}	$8.03^{+0.23}_{-0.26}$	$13.4^{0.7}_{-0.7}$	2400^{+9900}_{-1900}	$2.2^{+2.2}_{-1.7}$	—
Source_8†	31.8^{+7}_{-5}	$7.41^{+0.27}_{-0.34}$	$12.8^{+0.8}_{-0.7}$	670^{+2400}_{-550}	$3.2^{+1.2}_{-1.1}$	PM
Source_11†	29.2^{+8}_{-5}	$7.94^{+0.23}_{-0.26}$	$13.2^{+0.7}_{-0.7}$	1700^{+6300}_{-1300}	$2.4^{+2.3}_{-1.9}$	PM
Source_12†	36.0^{+6}_{-3}	$8.44^{+0.12}_{-0.13}$	$14.1^{+0.4}_{-0.3}$	12000^{+17000}_{-6000}	$3.3^{+0.7}_{-0.6}$	PM
Source_13⋆	26.2^{+6}_{-3}	$8.15^{+0.18}_{-0.19}$	$13.1^{+0.6}_{-0.5}$	1400^{+3800}_{-940}	$2.3^{+1.8}_{-1.5}$	—
Source_14	31.5^{+7}_{-5}	$8.59^{+0.17}_{-0.12}$	$14.3^{+0.4}_{-0.3}$	21000^{+33000}_{-11000}	$1.0^{+0.2}_{-0.1}$	PM
Source_16	35.5^{+13}_{-9}	$8.31^{+0.21}_{-0.20}$	$14.1^{+0.7}_{-0.7}$	13000^{+60000}_{-11000}	$1.9^{+0.5}_{-0.4}$	PL
Source_19†	31.3^{+8}_{-6}	$8.13^{+0.21}_{-0.20}$	$13.6^{+0.6}_{-0.6}$	3900^{+10000}_{-2900}	$2.3^{+0.6}_{-0.6}$	—
Source_20⋆	35.5^{+9}_{-7}	$7.80^{+0.28}_{-0.36}$	$13.5^{+0.7}_{-0.8}$	3400^{+14000}_{-2900}	$2.7^{+0.4}_{-0.5}$	PL
Source_23†	31.7^{+10}_{-7}	$8.17^{+0.22}_{-0.24}$	$13.7^{+0.7}_{-0.7}$	4900^{+20000}_{-3900}	$2.0^{+0.4}_{-0.4}$	—
Source_28†	39.4^{+11}_{-7}	$8.08^{+0.19}_{-0.21}$	$14.0^{+0.6}_{-0.6}$	9200^{+29000}_{-6700}	$3.3^{+0.7}_{-0.6}$	—
Source_29†	33.6^{+8}_{-4}	$8.13^{+0.14}_{-0.15}$	$13.8^{+0.5}_{-0.4}$	6000^{+13000}_{-3800}	$3.0^{+0.7}_{-0.6}$	—
Source_30	25.2^{+6}_{-3}	$8.19^{+0.21}_{-0.18}$	$13.3^{+0.6}_{-0.5}$	2000^{+5600}_{-1300}	$1.2^{+0.4}_{-0.3}$	PL
Source_33⋆	29.0^{+5}_{-5}	$8.06^{+0.18}_{-0.20}$	$13.4^{+0.5}_{-0.5}$	2500^{+5400}_{-1800}	$1.9^{+0.4}_{-0.4}$	PM
Source_34†	30.4^{+7}_{-5}	$7.70^{+0.25}_{-0.31}$	$13.1^{+0.7}_{-0.7}$	1100^{+4400}_{-920}	$2.7^{+0.6}_{-0.6}$	—
SPIRE-dropouts	57.1^{+16}_{-22}	$6.52^{+0.33}_{-0.41}$	$12.8^{+0.5}_{-0.7}$	700^{+1500}_{-560}	$6.7^{+2.4}_{-3.0}$	$z_{\rm free}$
	38.3^{+4}_{-5}	$6.71^{+0.19}_{-0.23}$	$12.5^{+0.4}_{-0.6}$	350^{+420}_{-250}	$4.0^{+0.1}_{-0.6}$	$z_{\rm fix}$

integrated autocorrelation time (τ) to evaluate the robustness of our MCMC analysis, where chain lengths of $> 50\tau$ should result in convergence. We calculate a typical integrated autocorrelation time of $\tau \sim 100$ steps, meaning our MCMC chains should obtain convergence. We discard the first 5000 steps, which is referred to as the 'burn-in' phase.

For the SPIRE-dropouts, we use the stacked SPIRE and SCUBA-2 fluxes stated in Table 3 to fit an average FIR SED for the SPIRE-dropout sample. We perform two sets of fits for the dropouts. For the first fit with the Ensemble Sampler, we use the same uninformative priors for $T_{\rm dust}$, β, and $\log_{10}(A)$ as before, but now add redshift as a free parameter with the following uninformative prior: $0 < z < 12$. The remaining steps are performed as before. In the second fit, we keep $T_{\rm dust}$, β, and $\log_{10}(A)$ as free parameters, but hold the redshift fixed to the MMPZ stacked photo-z estimate of $z = 4$.

In Fig. 9, we show the SEDs of 100 random samples for each SPIRE-detected source and for both stacked SPIRE-dropout runs, along with the best-fitting SED model.

4.2 Dust mass, FIR luminosity, and SFR

With the best-fitting SEDs in hand, we then estimate the dust mass ($M_{\rm dust}$), FIR luminosity ($L_{\rm FIR}$), and associated dust-obscured SFR for each SPIRE-detected source. We also calculate estimates for the stacked SPIRE-dropout sample. We estimate the dust mass using the following equation from D. A. Riechers et al. (2013):

$$M_{\rm dust} = S_\nu {D_L}^2 [(1+z)\kappa_\nu B_\nu(T)]^{-1} \tau_\nu [1-\exp(-\tau_\nu)]^{-1}, \quad (6)$$

where S_ν is the flux density at rest-frame 125 μm, D_L is the luminosity distance, κ_ν is the dust opacity coefficient, which is assumed to be 2.46 $\rm m^2 kg^{-1}$ at 125 μm (L. Dunne, S. A. Eales & M. G. Edmunds 2003; D. A. Riechers et al. 2013; J. Greenslade et al. 2020), and the redshift used for each source is stated in Table 5. The FIR luminosity is defined as the integrated luminosity from 42.5–122.5 μm (J. Greenslade et al. 2020). Using this FIR luminosity we finally calculate the dust-obscured SFR based on the conversion factor from D. A. Riechers et al. (2013), assuming a Chabrier IMF (G. Chabrier 2003).

In Table 5, we present the estimates for the characteristic dust temperature, dust mass, FIR luminosity and the corresponding dust-obscured SFR. These estimates are based on the 16th, 50th, and 84th percentiles of samples in the marginalized distributions. The estimates for the stacked SPIRE-dropouts represent the average physical properties of the total stacked SPIRE-dropout sample.

Based on our extracted results, we find that our SPIRE-detected sources have a mean FIR luminosity of $\log_{10}(L_{\rm FIR}/{\rm L}_\odot) = 13.6 \pm 0.1$ and a mean dust mass of $\log_{10}(M_{\rm dust}/{\rm M}_\odot) = 8.1 \pm 0.1$, where the uncertainty reflects the standard error on the mean of the SPIRE-detected sample. This identifies ~ 94 per cent of our SPIRE-detected sources as Hyper-Luminous IR galaxies (HyLIRGs; $L_{\rm FIR} > 10^{13}\,{\rm L}_\odot$), with corresponding dust-obscured SFRs on the order of thousands of solar masses per year (mean SFR $= 7000 \pm 1900\,{\rm M}_\odot{\rm yr}^{-1}$). Our FIR luminosity estimates probe higher luminosities compared to literature $L_{\rm IR}$ results (e.g. S. C. Chapman et al. 2005; C. M. Casey et al. 2012, 2013). However, our results agree well with the $L_{\rm FIR}$ estimates of J. Greenslade et al. (2020) who find a median of $L_{\rm FIR} \sim 10^{13.5}\,{\rm L}_\odot$, albeit our dust masses are on average an order of magnitude lower than their average of $\log_{10}(M_{\rm dust}/{\rm M}_\odot) = 9.1$. Compared to J. Cairns (2023), PhD Thesis,[5] we find a higher average $L_{\rm FIR}$ but a lower average dust mass by an order of magnitude. In comparison to both J. Greenslade et al. (2020) and J. Cairns (2023), the $L_{\rm FIR}$ range of our sample extends to much brighter sources ($L_{\rm FIR} > 10^{14}\,{\rm L}_\odot$) and hence probes higher average dust-obscured SFRs. The dust temperature of the SPIRE-detected sources lie between 20 and 40 K, which is encapsulated by the dust temperature range of the 850 μm-selected SMGs in S. C. Chapman et al. (2005).

Although the majority of sources in Table 5 are classified as HyLIRGs and therefore are expected to have high obscured SFRs, there are some sources that have excessively high SFRs ($> 10\,000\,{\rm M}_\odot{\rm yr}^{-1}$), namely Sources 4, 12, 14, and 16. Of these four, Source_4, Source_12, and Source_14 have been classified as potentially having multiplicity in optical/NIR bands. If these optical/NIR sources are indeed physically associated, the FIR source may be a blend of multiple shorter wavelength sources, and their high SFRs (and high FIR luminosities, $L_{\rm FIR} > 10^{14}\,{\rm L}_\odot$) may be a sign of interacting galaxies, or they may be groups or clusters of galaxies going through starbursts simultaneously (e.g. J. Greenslade et al. 2018; I. Oteo et al. 2018.) In particular, the *HST* cut-out of Source_12 reveals multiple sources located in a relatively compact region, which may suggest the presence of a galaxy group or cluster. Due to the multiple sources visible within the 850 μm beam for these sources, we cannot robustly identify a singular optical/NIR counterpart. In fact, if a cluster is present, the resulting dust-obscured SFR would be too high to assign to a singular source, but should be divided among multiple sources (I. Oteo et al. 2018).

Source 16, 20, and 30 are marked as potentially lensed, with the former having an estimated SFR $> 10\,000\,{\rm M}_\odot{\rm yr}^{-1}$, while the latter two do not have an unusually high SFR but could still be weakly lensed. Source_16 is categorized as having a consistent photo-z but the extracted $L_{\rm FIR}$ is suggestive of a lensing candidate, with $\log_{10}(L_{\rm FIR}/{\rm L}_\odot) = 14.1$.

Our stacked SPIRE-dropout population has a derived average redshift of $z = 6.7^{+2.4}_{-3.0}$, which is consistent within 1σ of the MMPZ redshift of the stacked fluxes, $z = 4.0^{+0.1}_{-0.6}$. However, the large error bars on the Emcee-derived redshift suggests there may be degeneracies or unexplored biases in the FIR SED fitting. At $z = 6.7$, we derive average properties of $\log_{10}(L_{\rm FIR}\,/\,{\rm L}_\odot) = 12.8^{+0.5}_{-0.7}$, $\log_{10}(M_{\rm dust}\,/\,{\rm M}_\odot) = 6.52^{+0.33}_{-0.41}$, and ${\rm SFR}_{\rm obsc} = 700^{+1500}_{-560}\,{\rm M}_\odot{\rm yr}^{-1}$. Using a fixed $z = 4$, we derive average properties of $\log_{10}(L_{\rm FIR}\,/\,{\rm L}_\odot) = 12.5^{+0.4}_{-0.6}$, $\log_{10}(M_{\rm dust}\,/\,{\rm M}_\odot) = 6.71^{+0.19}_{-0.23}$, and ${\rm SFR}_{\rm obsc} = 350^{+420}_{-250}\,{\rm M}_\odot{\rm yr}^{-1}$. The physical properties from the fixed and free z runs are all consistent within 1σ. We note that with a fixed $z = 4$, we derive a lower dust temperature and higher dust mass than at $z = 6.7$, due to the redshift-temperature degeneracy and the relation between dust temperature and dust mass. Our SFR and $L_{\rm FIR}$ result at $z = 6.7$ is comparable to that obtained by J. Greenslade et al. (2019) for their singular SPIRE-dropout source estimated to be at a similar redshift (SFR $\sim 500\,{\rm M}_\odot{\rm yr}^{-1}$ and $L_{\rm FIR} \sim 10^{12.7}\,{\rm L}_\odot$ at $z \sim 7$) however, our dust mass estimate falls ~ 2 orders of magnitude below their estimated range. Our $L_{\rm FIR}$ and SFR estimates from both SPIRE-dropout fits are consistent with the estimates of the extremely red SMGs ($z \geq 4$) studied in S. Ikarashi et al. (2017) that are also undetected with SPIRE. Our SFR values are almost an order of magnitude lower than almost all non-lensed $z > 4$ DSFGs in Y. Fudamoto et al. (2017) (see their table 7), which have an average SFR $\sim 3500\ {\rm M}_\odot{\rm yr}^{-1}$. Notably, the only SPIRE-dropout included in their comparison, HDF 850.1 (F. Walter et al. 2012), has a lensing-corrected SFR of $\sim 530\,{\rm M}_\odot{\rm yr}^{-1}$ using the magnification from R. Neri et al. (2014), consistent with our estimates. This supports the idea, also suggested by J. Greenslade et al. (2019), that SPIRE-dropouts may represent a more typical, fainter population of DSFGs at $z \geq 4$. Comparing our results with the properties of DSFGs listed in table 6 of Y. Fudamoto et al. (2017), our average SPIRE-dropout dust masses are ~ 2 orders of magnitude lower than their estimates (average of $\log_{10}(M_{\rm dust}/{\rm M}_\odot) \sim 9$). The inferred dust mass is strongly dependent on the assumed dust temperature due to the form of the modified blackbody equation. Specifically, for a fixed observed flux density, a higher dust temperature leads to a higher Planck function value, and thus a

[5] https://spiral.imperial.ac.uk/entities/publication/ffacffda-b6cb-4f85-bab3-0c53893e2dd5

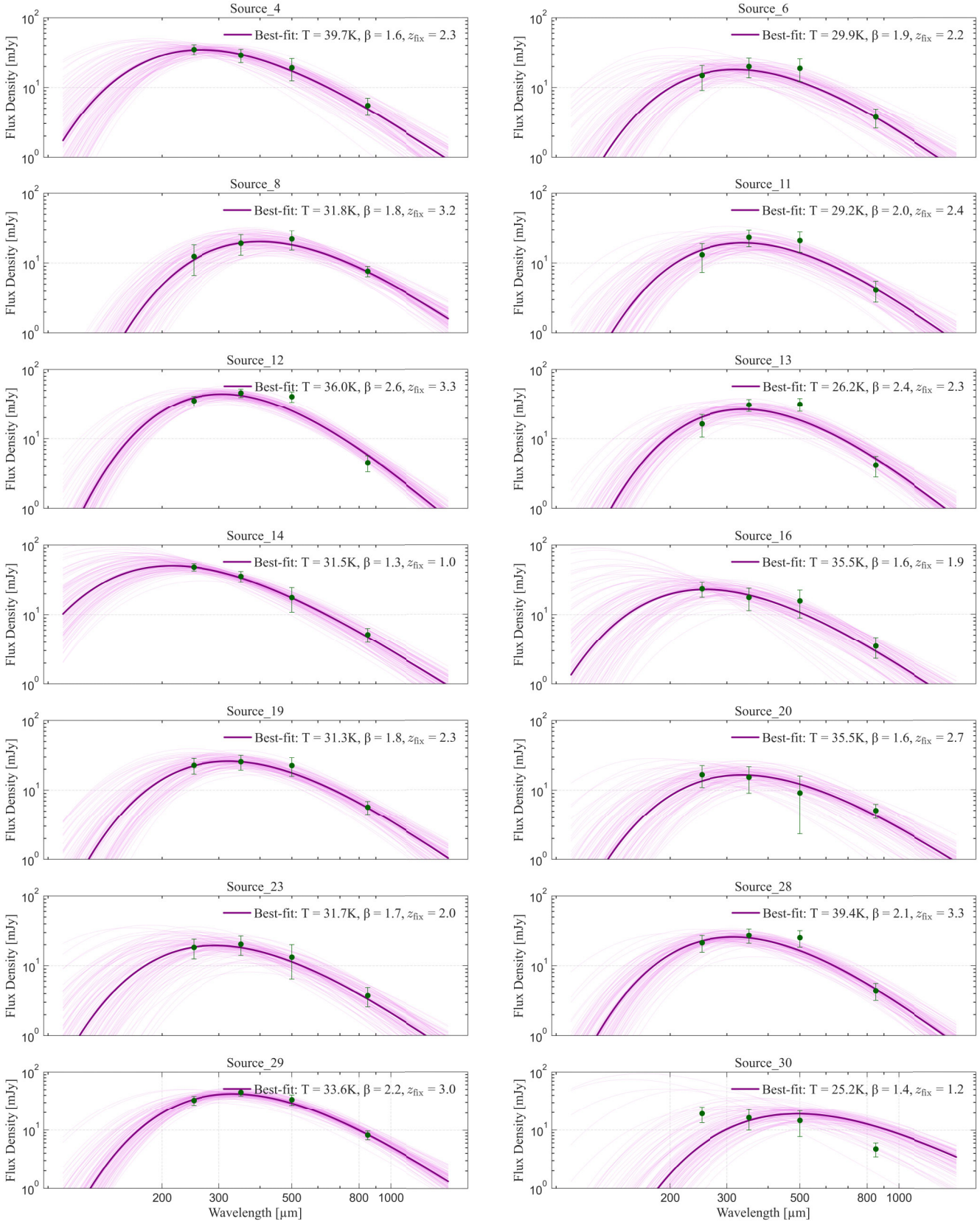

Figure 9. Resulting SED fits to the FIR fluxes from the `emcee` ensemble sampler. SEDs are for the SPIRE-detected sources; the last two SEDs are for the stacked SPIRE-dropout sample. The solid dark line in each plot shows the best fitting SED. The fainter, pink lines show 100 random samples. The data points mark the observed flux densities at 250, 350, 500 and 850 μm. Parameters (T, β) of the best-fitting SED are stated, as well as the redshift.

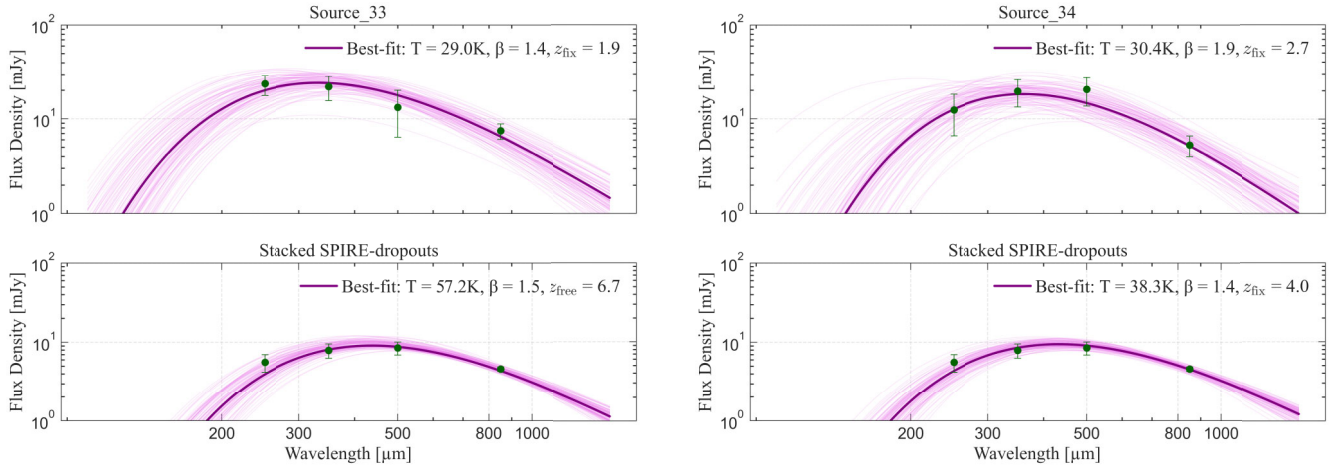

Figure 9. — *Continued*

Table 6. Derived SFRD of our SPIRE-detected sample (all), consistent photo-z SPIRE-detected sources and Stacked SPIRE-dropouts (with and without a fixed z.

z	SFRD	$\mathrm{SFRD_{min}}$ $[\mathrm{M_\odot yr^{-1}Mpc^{-1}}]$	$\mathrm{SFRD_{max}}$
		SPIRE-detected sample	
1–2	3.10×10^{-1}	2.12×10^{-1}	4.68×10^{-1}
2–3	4.35×10^{-1}	2.42×10^{-1}	8.49×10^{-1}
3–4	6.00×10^{-2}	4.07×10^{-2}	9.07×10^{-2}
		Consistent SPIRE-detected sample	
1–2	3.03×10^{-1}	2.08×10^{-1}	4.66×10^{-1}
		Stacked SPIRE-dropouts (free z)	
6–7	1.43×10^{-3}	1.14×10^{-3}	2.94×10^{-3}
		Stacked SPIRE-dropouts (fixed z)	
4–5	5.58×10^{-4}	1.56×10^{-4}	2.86×10^{-4}

lower dust mass is required to reproduce the observed emission. For our sample of stacked SPIRE-dropouts, we find a best-fitting dust temperature of $T_{\rm dust} = 57.1^{+16}_{-22}$ K at $z = 6.7$ from which we derive a dust mass of $\log_{10}(M_{\rm dust}/\mathrm{M_\odot}) = 6.52$. Propagating only the temperature uncertainties while keeping other parameters fixed, we find that increasing the temperature to 73.1 K lowers the dust mass to $\log_{10}(M_{\rm dust}/\mathrm{M_\odot}) = 6.2$, whereas decreasing the temperature to 35.1 K raises the dust mass to $\log_{10}(M_{\rm dust}/\mathrm{M_\odot}) = 7.1$. This inverse relation reflects the increased luminosity of warmer dust. Our median dust temperature is relatively high compared to other high-z dropout samples (e.g. Y. Fudamoto et al. 2017), which often assume or derive cooler dust. This may explain why our dust masses appear systematically lower. We note that, given the broad uncertainty on $T_{\rm dust}$ at $z = 6.7$, the dust mass is still at the lower end/falls below previous results. With a fixed $z = 4$, we derive $T_{\rm dust} = 38.3^{+3}_{-5}$ K and dust mass of $\log_{10}(M_{\rm dust}/\mathrm{M_\odot}) = 6.71$, the latter of which is higher than the $z = 6.7$ estimate but still falls below the literature results. To improve the dust temperature constraints for the dropouts, as well as for remaining SPIRE-detected SDF sources in general, we need extra data at high frequencies. In particular, the PRobe far-Infrared Mission for Astrophysics (PRIMA; A. Moullet et al. 2023) would be an ideal instrument to provide extra photometry at ~ 235 μm and shorter wavelengths with the Photometric Performance Indicator (PPI) bands to better constrain the peak and Wein side of the SED, and thus their dust properties. Six of the SPIRE-dropouts in our sample are flagged as potentially lensed (see Table 4). If confirmed, lensing would significantly affect the interpretation of their physical properties. Because lensing magnifies both flux and angular size, derived quantities such as SFR and dust mass may be overestimated when magnification is not taken into account. High-resolution imaging would be essential to confirm lensing, allowing refined estimates of their intrinsic properties.

4.3 Cosmic star formation rate density

We estimate the contribution of our SPIRE-detected sources and the average SPIRE-dropout population to the cosmic SFR density (SFRD) using the calculated SFRs in Table 5 and a $1/V_{\rm max}$ method (M. Schmidt 1968). Our results are tabulated in Table 6 and shown in Fig. 10.

We find that the SFRD values derived for the full SPIRE-detected sample (purple squares), particularly between $1 < z < 3$, are systematically higher than estimates from previous observational studies. Several factors likely contribute to this discrepancy. First, uncertainties in photometric redshift estimates, particularly for sources grouped with inconsistent photo-z/insufficient data may incorrectly place bright sources at lower redshifts, amplifying the derived SFRDs. To overcome this, we recalculate the SFRD using only SPIRE-detected sources with a consistent photo-z (teal circle) as defined in Table 4, which only marginally lowers the SFRD estimate at $1.5 < z < 2.5$, but we note that this decrease is partly a result of a lower source density, since without the inconsistent/insufficient sources, we are considering a smaller sample. Additionally, 88 per cent of the sources labelled as PM or PL in Table 4 are categorized as inconsistent or insufficient. Without confirmation of lensing or multiplicity for these sources, the SFRs of the individual 850 μm source is likely being overestimated. Higher resolution observations, e.g. with the SMA or NOEMA, will be crucial to refine the photometric redshifts and confirm any cases of lensing or multiplicity, leading to accurately characterized dust properties of our sample. Such observations are already underway.

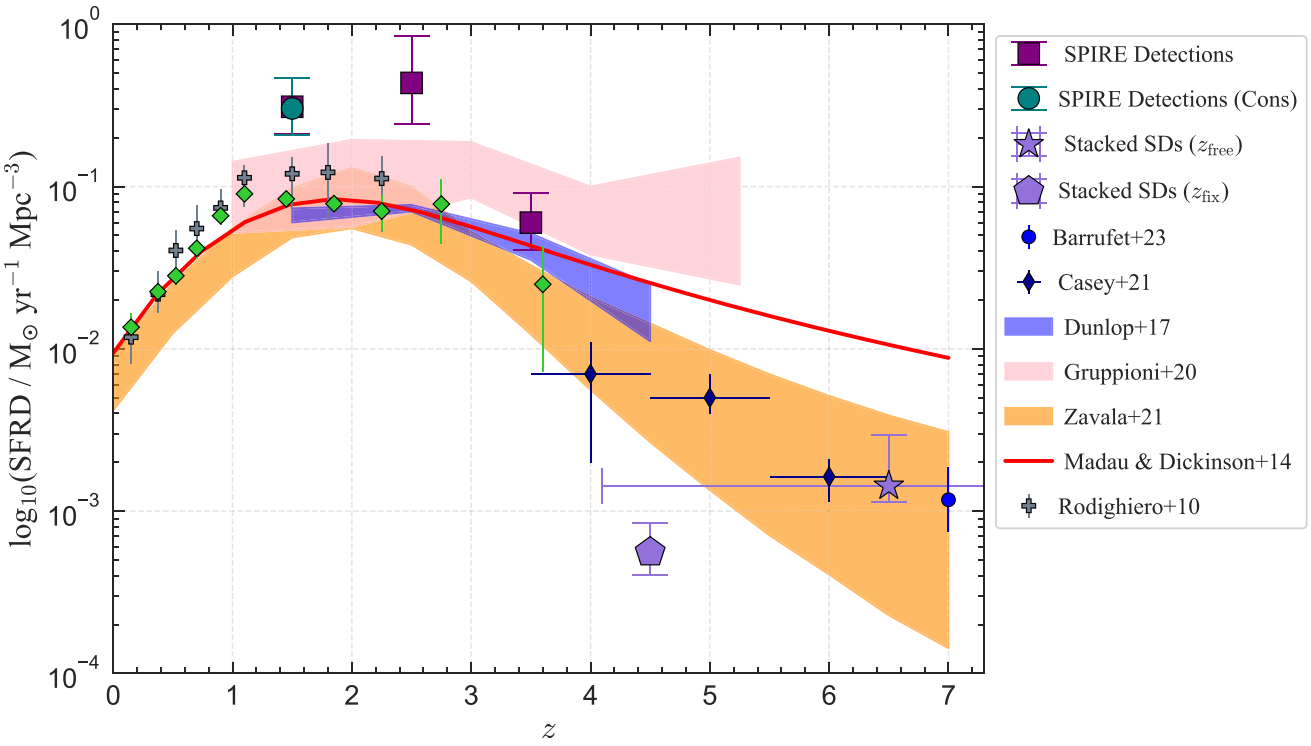

Figure 10. Contribution of all our SPIRE-detected sources from Table 5 (purple squares) and the average SPIRE-dropout population (star for free z and pentagon for fixed z) to the cosmic SFRD, compared with other literature results. We also show the SFRD when only considering SPIRE-detected sources with consistent photo-z from from Table 5 (teal circles). The solid red line shows the total SFRD from P. Madau & M. Dickinson (2014) and the orange region shows the dust-obscured SFRD from J. A. Zavala et al. (2021). The following literature results are also shown: G. Rodighiero et al. (2010), J. Dunlop et al. (2017), C. Gruppioni et al. (2020), C. M. Casey et al. (2021), J. A. Zavala et al. (2021), and L. Barrufet et al. (2023).

The presence of a local overdensity could also enhance the observed number of FIR-bright galaxies, potentially leading to an elevated SFRD relative to the cosmic average. The SPIRE number counts in the SDF, calculated by T. Varnish et al. (2025) using P(D) analysis, reveal a secondary bump at sub-mJy flux densities – approximately 0.5, 0.3, and 0.05 mJy at 250, 350, and 500 μm, respectively. The FIR colours of this bump suggest it originates from a population at redshift $z \sim 1$. This coincides with the excess seen in our SFRD, implying a potential physical association with the source population responsible for the SPIRE bump. Taken together, these results may point to the presence of a large-scale structure at $z \sim 1$, such as a forming galaxy cluster, similar to those reported in other studies that trace large-scale structure through overdensities of FIR or sub-mm sources (e.g. R. J. Ivison et al. 2013; D. Clements et al. 2014; E. E. Rigby et al. 2014). Confirming the redshift of our sources with spectroscopic observations and expanding our SFRD analysis to the entire 30 arcmin diameter SDF would confirm whether this potential physical association is real.

Our derived SFRD for the stacked SPIRE-dropouts is 14.7^{+30}_{-12} per cent of the total SFRD from P. Madau & M. Dickinson (2014) at $z = 6.7$. This is in agreement with the range of obscured SFRD predictions of J. A. Zavala et al. (2021) and L. Barrufet et al. (2023). The J. A. Zavala et al. (2021) models predict that most of the dust-obscured SF beyond $z = 4$ is due to ultra-luminous IR galaxies (ULIRGs; $L_{\rm FIR} > 10^{12}\,L_\odot$), which is consistent with the average luminosity of the stacked SPIRE-dropouts. Our SFRD result is also comparable to DSFGs in the millimetre-selected sample from C. M. Casey et al. (2012), who report a decline in the obscured SFRD over $4 < z < 6$. At a fixed redshift of $z = 4$, our SFRD estimate from the second Emcee run falls $\sim 7\sigma$ below the J. A. Zavala et al. (2021) results, suggesting a steeper decline in the SFRD at $z > 3$. This corresponds to a contribution of $1.83^{+2.8}_{-1.3}$ per cent to the total SFR density at $z = 4$. To precisely determine the contribution of the SPIRE-dropouts to the dust-obscured SFRD, we need a larger sample of SPIRE-dropouts to improve the statistics of our result; our SCUBA-2 data cover 28 per cent of the entire SDF. Given the unusually high fraction of SPIRE-dropouts in the Deep Region, SCUBA-2 coverage of the entire SDF would provide an improved sample of SPIRE-dropouts to study them further.

5 CONCLUSIONS

We present SCUBA-2 850 μm observations covering the central Deep Region of the *Herschel*-SPIRE Dark Field. We identify 36 sources of which 20 are categorized as SPIRE-dropouts; the remaining 16 make up our SPIRE-detected sample. We investigate the nature, evolution, and main physical properties of our SPIRE-detected and SPIRE-dropout samples. The main results of our work can be summarized as follows.

(i) Our 850 μm number counts are broadly consistent with existing literature, with minor deviations that are attributable to incompleteness and small-number statistics.

(ii) We cross-ID the 850 μm sources with multiwavelength data where available, ranging from optical to FIR wavelengths. Using these cross-IDs we estimate photo-z's for our sources using

MAGPHYS, BAGPIPES, and MMPZ. We categorize our sample based on whether all the estimates agree within the uncertainties (Consistent photo-z), do not agree within the uncertainties (Inconsistent photo-z), or if there are not enough data (Insufficient Data). We find that $>$ 50 per cent of our SCUBA-2 sources lack a robust optical/NIR counterpart primarily due to multiple candidate counterparts; these are grouped under 'Insufficient Data'. Three sources have consistent photo-z's and 13 have inconsistent photo-z's.

(iii) We identify the 850 μm-detected Source_29 as being associated with an optically-detected star. Using the *Gaia* parameters we estimate the IR excess of the star to be unphysical. We determine that the optical star is most likely a chance alignment with the FIR source. Ongoing submm observations will confirm this either way.

(iv) We determine whether there is a possibility of lensing based on an offset between the optical/NIR source and the FIR source. We classify nine sources as potentially lensed, while 15 sources are classified as potentially having multiplicity at shorter wavelengths. Higher resolution submm/mm data and spectroscopic observations would confirm our tentative classifications.

(v) Our photo-z analysis reveals the SPIRE-detected sample to lie primarily at $2 < z < 3$, while our SPIRE-dropouts favour higher redshifts ($z > 3$). Both these results are consistent with our analysis of their FIR/submm colours.

(vi) We extracted physical properties for our SPIRE-detected sample and stacked SPIRE-dropouts via FIR SED fitting. The SPIRE-detected sample yield average properties of $\log_{10}(L_{\rm FIR}\,/\,{\rm L}_\odot) = 13.6 \pm 0.1$, $\log_{10}(M_{\rm dust}\,/\,{\rm M}_\odot) = 8.10 \pm 0.1$, and ${\rm SFR}_{\rm obsc} = 7000 \pm 1900\,{\rm M}_\odot{\rm yr}^{-1}$. This suggests that 94 per cent of this sample are HyLIRGs. Our FIR luminosities generally agree with literature values but tend to extend to brighter luminosities and therefore higher SFRs. Our dust masses tend to fall below the values in the literature.

(vii) The extracted properties for the stacked SPIRE-dropouts yield $\log_{10}(L_{\rm FIR}\,/\,{\rm L}_\odot) = 12.8^{+0.5}_{-0.7}$, $\log_{10}(M_{\rm dust}\,/\,{\rm M}_\odot) = 6.52^{+0.33}_{-0.41}$, and ${\rm SFR}_{\rm obsc} = 700^{+1500}_{-560}\,{\rm M}_\odot{\rm yr}^{-1}$ at a derived redshift of $z = 6.7^{+2.4}_{-3.0}$. With a fixed $z = 4.0^{+0.1}_{-0.6}$, we extract average properties of $\log_{10}(L_{\rm FIR}\,/\,{\rm L}_\odot) = 12.5^{+0.4}_{-0.6}$, $\log_{10}(M_{\rm dust}\,/\,{\rm M}_\odot) = 6.71^{+0.19}_{-0.23}$, and ${\rm SFR}_{\rm obsc} = 350^{+420}_{-250}\,{\rm M}_\odot{\rm yr}^{-1}$. The redshift–dust temperature degeneracy prevents us from robustly constraining either of these parameters.

(viii) We estimate the contribution of the SPIRE-detected sources and stacked SPIRE-dropouts to the cosmic SFRD. The results of the SPIRE-detected sample show an excess from the literature results, particularly at $z \sim 1$. We suggest that this is associated with the secondary bump in the SPIRE number counts of this field at sub-mJy, which is also estimated to be at a similar redshift, hinting at the presence of a local overdensity in the SDF.

(ix) The stacked SPIRE-dropouts are estimated to account for $\sim$ 15 per cent of the total SFRD at $z = 6.7$, in agreement with literature values, and supports the predicted decline in SFRD at $z > 4$. If we assume the stacked photo-z of $z = 4$, the corresponding SFRD suggests a steeper decline in SFRD at $z > 3$ than literature results.

Overall, we conclude that while a fraction of our Deep Region sources have been constrained, future high-resolution submm/mm observations will be essential for resolving source multiplicity, identifying lensing candidates, and refining our understanding of the dust-obscured star-forming galaxy population at intermediate–high redshift. Recent high-resolution SMA observations at millimetre wavelengths for a subset of SDF sources will be presented in future work. At FIR wavelengths, future telescope concepts such as PRIMA will be ideal for probing the peak of the SED where it can provide tighter constraints, leading to improved estimates of physical properties.

ACKNOWLEDGEMENTS

The authors wish to thank the anonymous referee, whose detailed and insightful comments have vastly improved this manuscript. The James Clerk Maxwell Telescope is operated by the East Asian Observatory on behalf of The National Astronomical Observatory of Japan; Academia Sinica Institute of Astronomy and Astrophysics; the Korea Astronomy and Space Science Institute; the National Astronomical Research Institute of Thailand; Center for Astronomical Mega-Science (as well as the National Key R&D Program of China with No. 2017YFA0402700). Additional funding support is provided by the Science and Technology Facilities Council of the United Kingdom and participating universities and organizations in the United Kingdom and Canada. Additional funds for the construction of SCUBA-2 were provided by the Canada Foundation for Innovation. The authors wish to recognize and acknowledge the very significant cultural role and reverence that the summit of Maunakea has always had within the indigenous Hawaiian community. We are most fortunate to have the opportunity to conduct observations from this mountain. SPIRE has been developed by a consortium of institutes led by Cardiff University (UK) and including Univ. Lethbridge (Canada); NAOC (China); CEA, LAM (France); IFSI, Univ. Padua (Italy); IAC (Spain); Stockholm Observatory (Sweden); Imperial College London, RAL, UCL-MSSL, UKATC, Univ. Sussex (UK); and Caltech, JPL, NHSC, Univ. Colorado (USA). This development has been supported by national funding agencies: CSA (Canada); NAOC (China); CEA, CNES, CNRS (France); ASI (Italy); MCINN (Spain); SNSB (Sweden); STFC, UKSA (UK); and NASA (USA). AP acknowledges support from the Science and Technology Facilities Council (grant numbers ST/T506151/1, ST/V506734/1, and ST/W507519/1).

DATA AVAILABILITY

The raw SCUBA-2 data covering this field (450 and 850 μm) are publicly available in the JCMT archive at CADC, Project ID M18AP049 and M20AP045: https://www.cadc-ccda.hia-iha.nrc-cnrc.gc.ca/en/search/. The XID catalogue used in our cross-matching is from C. Pearson et al. (2025). The multiwavelength *Spitzer*-IRAC dark field catalogue is available in J. Krick et al. (2009) and references therein. Our final cross-matched SDF catalogue, described in Table A1, with optical–submm photometry is available in full online. Reduced data maps or any other data underlying this article will be shared upon reasonable request to the corresponding author.

REFERENCES

Álvarez-Márquez J. et al., 2023, A&A, 671, A105
Aravena M. et al., 2016, ApJ, 833, 68
Asboth V. et al., 2016, MNRAS, 462, 1989
Barger A. J., Cowie L. L., Sanders D. B., Fulton E., Taniguchi Y., Sato Y., Kawara K., Okuda H., 1998, Nature, 394, 248
Barrufet L. et al., 2023, MNRAS, 522, 3926
Battisti A. et al., 2019, ApJ, 882, 61
Boyajian T. S. et al., 2012, ApJ, 757, 112

Cairns J., 2023, PhD thesis, Imperial College London
Calzetti D., Armus L., Bohlin R. C., Kinney A. L., Koornneef J., Storchi-Bergmann T., 2000, ApJ, 533, 682
Capak P. L. et al., 2011, Nature, 470, 233
Carnall A., McLure R., Dunlop J., Davé R., 2018, MNRAS, 480, 4379
Casey C. M., 2020, ApJ, 900, 68
Casey C. M. et al., 2012, ApJ, 761, 140
Casey C. M. et al., 2013, MNRAS, 436, 1919
Casey C. M., Narayanan D., Cooray A., 2014, Phys. Rep., 541, 45
Casey C. M. et al., 2021, ApJ, 923, 215
Chabrier G., 2003, PASP, 115, 763
Chapin E. L., Berry D. S., Gibb A. G., Jenness T., Scott D., Tilanus R. P., Economou F., Holland W. S., 2013, MNRAS, 430, 2545
Chapman S. C., Blain A. W., Smail I., Ivison R. J., 2005, ApJ, 622, 772
Chen C.-C., Cowie L. L., Barger A. J., Casey C. M., Lee N., Sanders D. B., Wang W.-H., Williams J. P., 2013, ApJ, 776, 131
Cheng T. et al., 2019, MNRAS, 490, 3840
Clements D. et al., 2014, MNRAS, 439, 1193
Clements D. L. et al., 2010, A&A, 518, L8
Conley A. et al., 2011, ApJ, 732, L35
Coppin K. et al., 2006, MNRAS, 372, 1621
Cutri R. M. et al., 2013, Explanatory Supplement to the AllWISE Data Release Products
da Cunha E. et al., 2015, ApJ, 806, 110
Daddi E. et al., 2009, ApJ, 694, 1517
Devlin M. J. et al., 2009, Nature, 458, 737
Dole H. et al., 2006, A&A, 451, 417
Dowell C. D. et al., 2014, ApJ, 780, 75
Dunlop J. et al., 2017, MNRAS, 466, 861
Dunne L., Eales S. A., Edmunds M. G., 2003, MNRAS, 341, 589
Fazio G. et al., 2004, ApJS, 154, 10
Ford H. C. et al., 1998, in, Bely P. Y., Breckinridge J. B., eds, Proc. SPIE Conf. Ser. Vol. 3356 Space Telescopes and Instruments V. SPIE, Bellingham, p. 234
Foreman-Mackey D., Hogg D. W., Lang D., Goodman J., 2013, PASP, 125, 306
Fudamoto Y. et al., 2017, MNRAS, 472, 2028
Gaia Collaboration et al. 2023, A&A, 674, 1
Geach J. E. et al., 2017, MNRAS, 465, 1789
Greenslade J. et al., 2018, MNRAS, 476, 3336
Greenslade J. et al., 2019, MNRAS, 490, 5317
Greenslade J., Clements D. L., Petitpas G., Asboth V., Conley A., Pérez-Fournon I., Riechers D., 2020, MNRAS, 496, 2315
Griffin M. J. et al., 2010, A&A, 518, L3
Gruppioni C. et al., 2020, A&A, 643, A8
Hickox R. C. et al., 2012, MNRAS, 421, 284
Hodge J. et al., 2013, ApJ, 768, 91
Hsu L.-Y., Cowie L. L., Chen C.-C., Barger A. J., Wang W.-H., 2016, ApJ, 829, 25
Hughes D. H. et al., 1998, Nature, 394, 241
Hurley P. et al., 2017, MNRAS, 464, 885
Hyun M. et al. 2023. ApJS, 264, 19
Ikarashi S. et al., 2017, ApJ, 835, 286
Ivison R. et al., 2016, ApJ, 832, 78
Ivison R. J. et al., 2013, ApJ, 772, 137
Karim A. et al., 2013, MNRAS, 432, 2
Krick J. et al., 2009, ApJS, 185, 85
Madau P., Dickinson M., 2014, ARA&A, 52, 415
Magnelli B. et al., 2012, A&A, 539, A155
Moullet A. et al., 2023, preprint (arXiv:2310.20572)
Murakami H. et al., 2007, PASJ, 59, S369
Neri R., Downes D., Cox P., Walter F., 2014, A&A, 562, A35
Oliver S. J. et al., 2010, A&A, 518, L21
Onaka T. et al., 2007, PASJ, 59, S401
Oteo I. et al., 2018, ApJ, 856, 72
Pearson C. et al., 2017, Publ. Korean Astron. Soc., 32, 219
Pearson C., Varnish T., Wu X., Clements D., Parmar A., Davidge H., Pearson M., 2025, MNRAS, 539, 336
Pilbratt G. L. et al., 2010, A&A, 518, L1
Puget J. L., Abergel A., Bernard J. P., Boulanger F., Burton W. B., Desert F. X., Hartmann D., 1996, A&A, 308, L5
Riechers D. A. et al., 2010, ApJ, 720, L131
Riechers D. A. et al., 2013, Nature, 496, 329
Riechers D. A. et al., 2017, ApJ, 850, 1
Riechers D. A. et al., 2021, ApJ, 907, 62
Rieke G. et al., 2004, ApJS, 154, 25
Rigby E. E. et al., 2014, MNRAS, 437, 1882
Rodighiero G. et al., 2010, A&A, 515, A8
Savage R. S., Oliver S., 2007, ApJ, 661, 1339
Schmidt M., 1968, ApJ, 151, 393
Simcoe R., Metzger M., Small T., Araya G., 2000, BAAS, 196, 52
Simpson J. M. et al., 2014, AJ, 788, 125,
Simpson J. et al., 2019, ApJ, 880, 43
Smail I., Ivison R. J., Blain A. W., 1997, ApJ, 490, L5
Smolčić V. et al., 2012, A&A, 548, A4,
Varnish T., Wu X., Pearson C., Clements D., Parmar A., 2025, MNRAS, 539, 347
Viero M. P. et al., 2013, ApJ, 779, 32
Walter F. et al., 2012, Nature, 486, 233
Wardlow J. L. et al., 2011, MNRAS, 415, 1479
Weiß A. et al., 2009, ApJ, 707, 1201
Werner M. W. et al., 2004, ApJS, 154, 1
Wilson J. C. et al., 2003, in, Strojnik M., Andresen B. F., eds, Proc. SPIE Conf. Ser. Vol. 4841, Infrared Spaceborne Remote Sensing X. SPIE, Bellingham, p. 451
Windhorst R. A. et al., 2022, ApJ, 165, 13
Wyatt M. C., 2008, ARA&A, 46, 339
Zavala J. A. et al., 2021, ApJ, 909, 165

SUPPORTING INFORMATION

Supplementary data are available at *MNRAS* online.

Parmar2026_TableA1.csv

Please note: Oxford University Press is not responsible for the content or functionality of any supporting materials supplied by the authors. Any queries (other than missing material) should be directed to the corresponding author for the article.

APPENDIX A: SUMMARY OF FINAL CATALOGUE

The following is a summary of our final cross-ID catalogue, along with a description of each column. The full catalogue is available online.

Table A1. A list of all the columns in our final cross-ID catalogue and a description of each one. All magnitudes are given in the AB magnitude system. Any magnitudes or fluxes in the final catalogue preceded with a '>' marks that magnitude/flux as a non-detection (i.e. has a $< 5\sigma$ significance). These non-detections are not used to estimate the photo-z estimates of our sources in Section 3.4 unless specifically stated otherwise.

Column Name	Description	Units
Source name	ID of source	–
RA (deg)	Right ascension of 850 μm source	degrees
Dec. (deg)	Declination of 850 μm source	degrees
IRAC_ID	ID of counterpart from IRAC Dark Field Catalogue of J. Krick et al. (2009)	–
u_mag	Palomar Hale LFC *u'*-band magnitude	mag
u_mag_err	Palomar Hale LFC *u'*-band magnitude error	mag
g_mag	Palomar Hale LFC *g'*-band magnitude	mag
g_mag_err	Palomar Hale LFC *g'*-band magnitude error	mag
r_mag	Palomar Hale LFC *r'*-band magnitude	mag
r_mag_err	Palomar Hale LFC *r'*-band magnitude error	mag
acs_mag	*HST* ACS-WFC *F*814*W* magnitude	mag
acs_mag_err	*HST* ACS-WFC *F*814*W* magnitude error	mag
z_mag	Palomar Hale LFC *z'*-band magnitude	mag
z_mag_err	Palomar Hale LFC *z'*-band magnitude error	mag
irac1_flux_μJy	*Spitzer*-IRAC 3.6 μm flux	μJy
irac1_fluxerr_μJy	*Spitzer*-IRAC 3.6 μm flux error	μJy
irac2_flux_μJy	*Spitzer*-IRAC 4.5 μm flux	μJy
irac1_fluxerr_μJy	*Spitzer*-IRAC 4.5 μm flux erro	μJy
irac3_flux_μJy	*Spitzer*-IRAC 5.8 μm flux	μJy
irac3_fluxerr_μJy	*Spitzer*-IRAC 5.8 μm flux error	μJy
irac4_flux_μJy	*Spitzer*-IRAC 8 μm flux	μJy
irac4_fluxerr_μJy	*Spitzer*-IRAC 8 μm flux error	μJy
Akari11_flux_μJy	AKARI 11 μm flux	μJy
Akari11_fluxerr_μJy	AKARI 11 μm flux error	μJy
Akari15_flux_μJy	AKARI 15 μm flux	μJy
Akari15_fluxerr_μJy	AKARI 15 μm flux error	μJy
Akari18_flux_μJy	AKARI 18 μm flux	μJy
Akari18_fluxerr_μJy	AKARI 18 μm flux error	μJy
XID_ID	ID of counterpart from XID MIPS Dark Field Catalogue of C. Pearson et al. (2025)	–
mips24_flux_μJy	*Spitzer*-MIPS 24 μm flux	μJy
mips24_fluxerr_μJy	*Spitzer*-MIPS 24 μm flux error	μJy
spire250_flux_mJy	*Herschel*-SPIRE 250 μm flux	mJy
spire250_fluxerr_mJy	*Herschel*-SPIRE 250 μm flux error	mJy
spire350_flux_mJy	*Herschel*-SPIRE 350 μm flux	mJy
spire350_fluxerr_mJy	*Herschel*-SPIRE 350 μm flux error	mJy
spire500_flux_mJy	*Herschel*-SPIRE 500 μm flux	mJy
spire500_fluxerr_mJy	*Herschel*-SPIRE 500 μm flux error	mJy
scuba2_450_flux_mJy	SCUBA-2 450 μm flux	mJy
scuba2_450_fluxerr_mJy	SCUBA-2 450 μm flux error	mJy
scuba2_850_flux_mJy	SCUBA-2 850 μm flux	mJy
scuba2_850_fluxerr_mJy	SCUBA-2 850 μm flux error	mJy
peak_snr_850	SCUBA-2 850 μm SNR	–

This paper has been typeset from a TEX/LATEX file prepared by the author.